Nonequilibrium steady states of electric field driven Mott insulators

Yuta Murakami and Philipp Werner
Department of Physics, University of Fribourg, 1700 Fribourg, Switzerland

(Received 23 April 2018; revised manuscript received 1 July 2018; published 2 August 2018)

We present a systematic study of the nonequilibrium steady states (NESS) in Mott insulators driven by dc or ac electric fields, based on the Floquet dynamical mean-field theory. The results are analyzed using a generalized tunneling formula for the current, which is reminiscent of the Meir-Wingreen formula and provides insights into the relevant physical processes. In the dc case, the spectrum of the NESSs exhibits Wannier-Stark (WS) states associated with the lower and upper Hubbard bands. In addition, there emerge WS sidebands from many-body states. Using the tunneling formula, we demonstrate that the tunneling between these WS states leads to peaks or humps in the induced dc current. In the ac case, we cover a wide parameter range of excitation frequencies and field strengths to clarify the crossover from field-induced tunneling behavior in the dc limit to nonequilibrium states dominated by multiphoton absorption in the ac limit. In the crossover regime, the single-particle spectrum is characterized by a coexistence of Floquet sidebands and WS peaks, and the current and double occupation exhibit a nontrivial dependence on the field strength. The tunneling formula works quantitatively well even in the ac case, and we use it to discuss the potential cooperation of tunneling and multiphoton processes in the crossover regime. The tunneling formula and its simplified versions also provide physical insights into the high-harmonic generation in Mott insulators.

DOI: 10.1103/PhysRevB.98.075102

I. INTRODUCTION

Pump-probe spectroscopy has become a versatile tool for the investigation of nonequilibrium effects in correlated materials [1]. In these experiments, the material is driven out of equilibrium by a strong laser pulse (pump), and its properties during or after the applied field pulse are measured by weaker probe pulses. Since the hopping times in typical correlated solids are of the order of femtoseconds, THz field pulses may be regarded as quasistatic fields, while optical pulses induce interband transitions or so-called Floquet states with time-averaged properties that may differ from those of equilibrium states [2].

Mott insulators are strongly correlated materials, where nonequilibrium phase transitions induced by both types of excitations have been extensively studied. These systems would be metallic according to band theory but are insulating in equilibrium because the charge motion is blocked by strong Coulomb interactions. Photo-induced phase transitions to a nonthermal metal state by 1.55-eV laser pulses have been demonstrated in organic materials [3,4], a nickel chain compound [5], and cuprates [6], while a dielectric breakdown using (quasi)static fields has recently been observed in Sr_2CuO_2 [7], VO_2 [8], and an organic molecular compound [9]. These complementary types of field-induced phase transitions have also been studied theoretically in one-dimensional models using analytical methods, exact diagonalization, and time-dependent density matrix renormalization group calculations [10–19], in two-dimensional models [10,20], and in higher dimensions using time-dependent Gutzwiller [21] and nonequilibrium dynamical mean-field calculations [22–28]. While these works have provided important insights into the nonequilibrium dynamics of Mott insulators in strong fields, such as the threshold behavior of the field-induced current in the dielectric breakdown case or the energy distribution of photo-doped carriers after a resonant excitation, we still lack a systematic investigation of the general case where both the field amplitude and driving frequency are of the order of the characteristic energy scales of the system.

Even though previous studies have mainly focused on transient dynamics and isolated interacting systems are expected to heat up to infinite temperature under continuous driving [29,30], it should be noted that recent theoretical works have shown that long-lived quasisteady states (prethermal states) can be rapidly reached, both in the case of near-resonant driving [27,28] and in the static limit [22,25], and that the characteristic properties of Floquet states are induced already by few-cycle pulses [31]. In addition, realistic systems are coupled to an environment and the energy injected by the field can be dissipated. In this case, the system does not reach the infinite temperature state, but instead approaches a stable Floquet nonequilibrium steady state (NESS) under continuous driving [32]. Thus, for a better understanding of strong field effects in Mott insulators driven by a pump pulse, it is useful to perform a systematic investigation of the properties of these NESSs. So far, the NESSs of Mott insulating systems have been investigated in the dc limit [32–38] and some ac regimes [34,39–42], but the general features in the two-dimensional space of driving frequency and driving amplitude remain to be revealed.

In this paper, we provide a systematic study of the NESS properties of the electric-field-driven Mott-insulating Hubbard model using a Floquet implementation of dynamical mean-field theory (Floquet DMFT) [34,40,43,44]. In order to stabilize a true NESS, this formalism involves a coupling to a heat bath, which here consists of free fermions. While the

parameters of the heat bath have an effect on the NESSs, we discuss qualitative features which are robust against the choice of bath parameters. The Floquet DMFT is implemented with the noncrossing approximation (NCA) as an impurity solver, which is reliable in the strong-coupling regime. Hence our analysis mainly focuses on systems with a large Coulomb interaction U, i.e., deep in the Mott regime.

In the dc limit, we show that our setup reproduces the qualitative results of the previous studies on isolated systems, such as Wannier-Stark states and the associated resonances in the field-induced current [25]. Furthermore, we reveal additional WS states connected to many-body processes that are different from the usual Hubbard band resonances. In the ac case, we study a wide parameter range covering the near-dc limit and the weak-field ac limit and discuss the behavior of the spectral function, induced current, and double occupation in the crossover regime which connects these two limits. In order to obtain physical insights into the involved processes, we also introduce a generalized tunneling formula, which is applicable both to the dc and ac cases. We demonstrate that this formula is also useful to investigate the high-harmonic generation (HHG) in Mott insulators.

The paper is organized as follows. In Sec. II, we explain the Floquet DMFT implemented with the noncrossing approximation (NCA) as an impurity solver [42,45]. Furthermore, we introduce the generalized tunneling formula for the current in NESSs and its simplified versions. In Sec. III, we discuss the properties of NESSs induced by dc fields, while in Sec. IV, we analyze the NESSs induced by ac fields and discuss HHG based on the tunneling formula. Section V contains a summary and conclusions.

II. FORMALISM

A. Model: Hubbard model coupled to a heat bath

We consider the half-filled Hubbard model attached to a thermal bath and driven by an electric field,

$$H(t) = -\sum_{\langle i,j\rangle,\sigma} v_{ij}(t) c^{\dagger}_{i,\sigma} c_{j,\sigma} + U \sum_{i} n_{i\uparrow} n_{i\downarrow} - \mu \sum_{i} n_i + H_{\rm bath}. \quad (1)$$

Here $c^{\dagger}_{i,\sigma}$ is the creation operator of an electron with spin σ at the site i, U is the onsite Coulomb interaction, v_{ij} is the hopping parameter, and μ is the chemical potential. The sum in the hopping term is over nearest-neighbor sites $\langle i,j\rangle$. The effect of the electric field is introduced by the Peierls substitution, $v_{ij}(t) = v_{ij} \exp(-iq \int_{\mathbf{r}_i}^{\mathbf{r}_j} d\mathbf{r}\mathbf{A}(t))$, where the vector potential $\mathbf{A}(t)$ is related to the electric field by $\mathbf{E}(t) = -\partial_t \mathbf{A}(t)$ (temporal gauge). Here q is the electron charge. We consider a hypercubic lattice with lattice spacing a in the limit of infinite spatial dimensions ($v = \frac{v^*}{2\sqrt{d}}$ with $d \to \infty$), which has a Gaussian density of states $\rho(\epsilon) = \frac{1}{\sqrt{\pi} v^*} \exp[-\epsilon^2/v^{*2}]$. In the following, we set $q, a = 1$ and use v^* as the unit of energy. As for the interaction, we mainly focus on a large-gap Mott insulator with $U = 8$, which is consistent with use of NCA. $H_{\rm bath}$ describes the coupling of the system to the environment (open system). We use a free electron bath (the Büttiker model), with a finite band width $W_{\rm bath}$, whose retarded self-energy is $-{\rm Im}\Sigma^R_{\rm bath}(\omega) = \Gamma\sqrt{1-(\omega/W_{\rm bath})^2}$. The Keldysh and advanced components can be obtained from this by the fluctuation-dissipation theorem [43,44].

In the present study, we apply the dc and ac fields along the body diagonal, $\mathbf{A}(t) = A(t)\mathbf{e}_0$ with $\mathbf{e}_0 = (1,1,\ldots,1)$. In both cases, the system reaches a nonequilibrium steady state (NESS) in which the excitation by the field is balanced by the dissipation to the thermal bath. To be precise, in the dc case, the time-dependent vector potential is $qaA(t) = \Omega t$, corresponding to the field strength $E_0 = -\frac{\Omega}{qa}$. In this gauge $H(t)$ oscillates with frequency Ω, but the NESS exhibits no time dependence of the physical observables. On the other hand, for the ac field, we use $qaA(t) = A_0 \sin\Omega t$ so that the field strength along a given axis is $E(t) = -\frac{A_0}{qa}\Omega\cos\Omega \equiv -E_0\cos\Omega t$. In this case, the NESS is time periodic with a period of $\mathcal{T} = \frac{2\pi}{\Omega}$.

B. Method: Floquet DMFT

Since in both the dc and ac field cases, the time-dependent Hamiltonian is time periodic, we can use the Floquet dynamical mean-field theory (FDMFT) to describe the NESSs. This formalism uses Floquet Green's functions in the DMFT self-consistency loop [33–35,39–42,44,46]. Detailed explanations on FDMFT can be found in previous articles [34,43,44], so we only briefly explain the formalism here.

When we are interested in transient dynamics starting from an equilibrium state at some time t_0, we define the Green's functions on the so-called Kadanoff-Baym contour. They can be expressed in terms of the Matsubara, left-mixing, right-mixing, lesser, greater, retarded, and advanced components [43]. For the NESSs in an open system under periodic driving, the initial correlations are irrelevant. Hence, one can neglect the Matsubara, left-mixing, and right-mixing components and take $t_0 \to -\infty$, which reduces the problem to the Keldysh formalism.

In the Keldysh formalism, the electron Green's function $G(t,t') \equiv -i\langle \mathcal{T}_{\mathcal{C}_K} c(t) c^{\dagger}(t')\rangle$ is defined on the Keldysh contour $\mathcal{C}_K = \mathcal{C}_1 \cup \mathcal{C}_2$, where $\mathcal{C}_1 = [-\infty,\infty]$ and $\mathcal{C}_2 = [\infty,-\infty]$. Here $\mathcal{T}_{\mathcal{C}_K}$ is the contour ordering operator and $\langle\cdots\rangle$ indicates the average with respect to some initial ensemble. A straightforward expression for the Green's function in this formalism is

$$\check{G}(t,t') \equiv \begin{bmatrix} G^{11}(t,t') & G^{12}(t,t') \\ G^{21}(t,t') & G^{22}(t,t') \end{bmatrix}. \quad (2)$$

Here $G^{ij}(t,t')$ indicates $t \in \mathcal{C}_i$ and $t' \in \mathcal{C}_j$. The physical representation for the Green's function is defined as

$$\underline{G} \equiv \begin{bmatrix} G^R & G^K \\ 0 & G^A \end{bmatrix} = \check{L}\check{\sigma}_3\check{G}\check{L}^{\dagger} \text{ with } \check{L} = \tfrac{1}{\sqrt{2}}\begin{bmatrix} 1 & -1 \\ 1 & 1 \end{bmatrix}, \quad (3)$$

where $\check{\sigma}_3$ is the third Pauli matrix. R, A, and K stand for the retarded, advanced, and Keldysh components, respectively (the Larkin-Ovchinnikov form). The effect of the interaction on the Green's function is taken into account through the self-energy Σ. The corresponding Dyson equation is

$$\int_{-\infty}^{\infty} dt_1 \left[\underline{G}_0^{-1}(t,t_1) - \underline{\Sigma}(t,t_1)\right]\underline{G}(t_1,t') = \underline{I}\delta(t-t') \quad (4)$$

in the Larkin-Ovchinnikov form. Here G_0 indicates the Green's function of the free electron (no interaction) system, G_0^{-1} is the inverse function of it, and I is the identity matrix.

So far, the Green's functions and the self-energies are expressed as functions of two times (the two-time representation). On the other hand, in the present case of time-periodic NESSs, all these two-time quantities should be time periodic with respect to the averaged time: $F(t,t') = F(t+\mathcal{T},t'+\mathcal{T})$ or $F(t_\mathrm{r};t_\mathrm{av}) = F(t_\mathrm{r};t_\mathrm{av}+\mathcal{T})$. Here $t_\mathrm{r} = t-t'$ and $t_\mathrm{av} = \frac{t+t'}{2}$. Because of this periodicity, one can introduce the Floquet representation of these functions as

$$\mathbf{F}_{mn}(\omega) \equiv \frac{1}{\mathcal{T}}\int_0^{\mathcal{T}} dt_\mathrm{av}\int_{-\infty}^{\infty} dt_\mathrm{r} \times e^{i(\omega+\frac{m+n}{2}\Omega)t_\mathrm{r}} e^{i(m-n)\Omega t_\mathrm{av}} F(t_\mathrm{r};t_\mathrm{av}). \tag{5}$$

In this form, one can regard a function as a collection of matrices for different ω. This expression is very useful since the Dyson equation in the two-time representation, Eq. (4), becomes a matrix multiplication at each ω,

$$\left[\underline{\mathbf{G}}_0^{-1}(\omega) - \underline{\Sigma}(\omega)\right]\cdot\underline{\mathbf{G}}(\omega) = \underline{\mathbf{I}}, \tag{6}$$

where a bold letter indicates the Floquet representation of the corresponding function, the underline indicates the Larkin-Ovchinnikov form.

Now the question is how to obtain the electron self-energy. For this, we employ DMFT. The main idea of DMFT is to evaluate the electron Green's function and self-energy by mapping the original lattice problem to an effective impurity problem [47], whose action can be expressed as

$$\mathcal{S}_\mathrm{imp} = \mathcal{S}_\mathrm{loc} + \mathcal{S}_\mathrm{hyb}, \tag{7a}$$

$$\mathcal{S}_\mathrm{loc} = -i\int_\mathcal{C} dt\, H_\mathrm{loc}[d^\dagger(t),d(t)], \tag{7b}$$

$$\mathcal{S}_\mathrm{hyb} = -i\int_\mathcal{C} dt_1 dt_2 \sum_\sigma d_\sigma^\dagger(t_1)\Delta(t_1,t_2)d_\sigma(t_2). \tag{7c}$$

Here $d_\sigma^\dagger$ is the creation operator at the impurity site with spin σ; H_loc is identical to the local part of the lattice model and includes the local Hubbard interaction and the chemical potential. Δ is the hybridization function, and we assume that the spin-up and spin-down components are symmetric. For the NESSs, the hybridization function is also time periodic, so that the Floquet representation can be introduced. The hybridization function is self-consistently determined in such a way that the local lattice Green's function

$$G_\mathrm{loc}(t,t') = -i\langle \mathcal{T}_{\mathcal{C}_K} c_{i,\sigma}(t)c_{i,\sigma}^\dagger(t')\rangle \tag{8}$$

is equal to the Green's function of the impurity site, and the (momentum-independent) self-energy of the lattice is identical to the self-energy of the impurity problem. Here we also assume a homogeneous system.

As depicted in Fig. 1, the DMFT solution is obtained by iterating a self-consistency loop for a given impurity solver. The first thing to note is that, in FDMFT, we introduce the Floquet representation for the relevant functions and we use them to solve the Dyson equation both for the lattice model and the effective impurity model. In the present study, we employ an impurity solver based on the noncrossing approximation (NCA). This is the lowest order self-consistent expansion in the hybridization function Δ, which is expected to produce qualitatively correct results deep in the Mott phase [45]. To evaluate the (pseudoparticle) self-energies in NCA, we use the two-time representation of the Green's functions. The transformation between the Floquet representation and the two-time representation is implemented using fast Fourier transformations. Detailed explanations of the NCA solver for nonequilibrium impurity problems can be found in Ref. [45] and the supplemental material of Ref. [42]. We also note that the effect of the field enters through the time-periodic kinetic energy $\epsilon_\mathbf{k}(t) = \epsilon(\mathbf{k}-\mathbf{A}(t))$, which appears in the lattice Dyson equation; see the left part of Fig. 1.

C. Observables

The observables used in this paper are defined as follows. We are interested in the time-averaged local single-particle spectra,

$$\bar{A}_\mathrm{loc}(\omega) = -\frac{1}{\pi}\mathrm{Im}\frac{1}{\mathcal{T}}\int_0^{\mathcal{T}} dt_\mathrm{av}\int dt_\mathrm{r} e^{i\omega t_\mathrm{r}} G^R_\mathrm{loc}(t_\mathrm{r};t_\mathrm{av}). \tag{9}$$

The time-averaged occupancy of the energy levels is given by

$$\bar{N}_\mathrm{loc}(\omega) = \frac{1}{2\pi}\mathrm{Im}\frac{1}{\mathcal{T}}\int_0^{\mathcal{T}} dt_\mathrm{av}\int dt_\mathrm{r} e^{i\omega t_\mathrm{r}} G^<_\mathrm{loc}(t_\mathrm{r};t_\mathrm{av}), \tag{10}$$

where $<$ indicates the lesser part of the Green's function. The distribution function is defined as $\bar{f}(\omega) = \bar{N}_\mathrm{loc}(\omega)/\bar{A}_\mathrm{loc}(\omega)$. In the dc case, we do not need to take time averages and just write A_loc, N_loc, and f.

The doublon density, the current, and the kinetic energy are measured as

$$d(t) = \langle n_{i,\uparrow}(t)n_{i,\downarrow}(t)\rangle, \tag{11}$$

$$j(t) = \frac{q}{N}\sum_{\mathbf{k},\sigma}\mathbf{e}_0\cdot\mathbf{v}_\mathbf{k}(t)\langle c^\dagger_{\mathbf{k},\sigma}(t)c_{\mathbf{k},\sigma}(t)\rangle, \tag{12}$$

$$E_\mathrm{kin}(t) = \frac{1}{N}\sum_{\mathbf{k},\sigma}\epsilon_\mathbf{k}(t)\langle c^\dagger_{\mathbf{k},\sigma}(t)c_{\mathbf{k},\sigma}(t)\rangle. \tag{13}$$

Here N is the system size, $\mathbf{k}$ is the lattice momentum, $c^\dagger_{\mathbf{k},\sigma} = \frac{1}{\sqrt{N}}\sum_i e^{i\mathbf{k}\cdot\mathbf{r}_i}c^\dagger_{i,\sigma}$, and $\mathbf{v}_\mathbf{k}(t) = \partial_\mathbf{k}\epsilon(\mathbf{k}-\mathbf{A}(t))$. Let us also introduce another expression for the current in terms of $G_\mathbf{k}(t,t') = -i\langle\mathcal{T}_\mathcal{C} c_{\mathbf{k},\sigma}(t)c^\dagger_{\mathbf{k},\sigma}(t')\rangle$, namely

$$\begin{aligned} j(t) &= i\frac{q}{N}\sum_\alpha\sum_{\mathbf{k},\sigma}\epsilon_\mathbf{k}(t)\left[\partial_{k_\alpha}G^<_\mathbf{k}(t,t)\right] \\ &= i\frac{q}{N}\sum_{\mathbf{k},\sigma}\epsilon_\mathbf{k}(t)\int_{-\infty}^{t} d\bar{t}\left[\sum_\alpha\partial_{k_\alpha}\epsilon_\mathbf{k}(t)\right] \\ &\quad\times\left[G^>_\mathbf{k}(t,\bar{t})G^<_\mathbf{k}(\bar{t},t) - G^<_\mathbf{k}(t,\bar{t})G^>_\mathbf{k}(\bar{t},t)\right]. \end{aligned} \tag{14}$$

To derive this expression, we use partial integration from Eq. (12) and the formula

$$\partial_{k_\alpha}G_\mathbf{k}(t,t') = \int_{\mathcal{C}_K} d\bar{t}\,G_\mathbf{k}(t,\bar{t})[\partial_{k_\alpha}\epsilon_\mathbf{k}(\bar{t})]G_\mathbf{k}(\bar{t},t'), \tag{15}$$

where $\int_{\mathcal{C}_K}$ is the contour integral along the Keldysh contour. The latter expression can be derived by taking the derivative

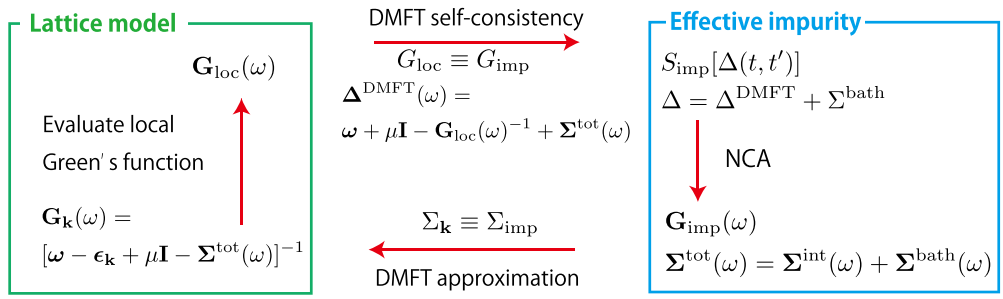

FIG. 1. FDMFT self-consistency loop. Bold letters indicate the Floquet representation of the corresponding function. $S_{\rm imp}$ is the impurity action, which is determined by the hybridization function (Δ). In the present case, the hybridization function consists of the effective bath which mimics the surrounding lattice ($\Delta^{\rm DMFT}$) and the attached electron bath ($\Sigma^{\rm bath}$). The problem is solved by NCA, which yields the impurity Green's function ($G_{\rm imp}$) and the self-energy ($\Sigma^{\rm tot}$) consisting of the contribution from the interaction ($\Sigma^{\rm int}$) and that from the bath ($\Sigma^{\rm bath}$). Using the self-energy and $\epsilon_{\mathbf{k}}(t) = \epsilon(\mathbf{k} - \mathbf{A}(t))$, we obtain the lattice Green's function at each momentum, and by averaging over $\mathbf{k}$, we obtain the local Green's function. Through the impurity Dyson equation, we update the hybridization function.

with respect to $\mathbf{k}$ of the Dyson equation and assuming a momentum-independent self-energy ($G_{\mathbf{k}}^{-1} = G_{0,\mathbf{k}}^{-1} - \Sigma$).

In the present case of a hypercubic lattice and an electric field pointing in the body-diagonal direction, the momentum ($\mathbf{k} = (k_1, k_2, \ldots, k_d)$) dependence of the Green's function can be parameterized by $\epsilon = -2v\sum_{i=1}^{d}\cos(k_i)$ and $\bar{\epsilon} = -2v\sum_{i=1}^{d}\sin(k_i)$, i.e., $G_{\mathbf{k}}(t,t') = G_{\epsilon,\bar{\epsilon}}(t,t')$. Using this, one can express the current as

$$j(t) = -\frac{q}{2}\int d\epsilon d\bar{\epsilon}\rho(\epsilon,\bar{\epsilon})\int_{-\infty}^{t} d\bar{t}\mathcal{F}(\epsilon,\bar{\epsilon},t,\bar{t}) \times [G^{>}_{\epsilon,\bar{\epsilon}}(t,\bar{t})G^{<}_{\epsilon,\bar{\epsilon}}(\bar{t},t) - G^{<}_{\epsilon,\bar{\epsilon}}(t,\bar{t})G^{>}_{\epsilon,\bar{\epsilon}}(\bar{t},t)], \quad (16)$$

with

$$\mathcal{F}(\epsilon,\bar{\epsilon},t,\bar{t}) = [(\epsilon^2+\bar{\epsilon}^2)e^{i(A(t)-A(\bar{t}))} - \text{H.c.} - (\epsilon - i\bar{\epsilon})^2 e^{i(A(t)+A(\bar{t}))} - \text{H.c.}]. \quad (17)$$

Here $\rho(\epsilon,\bar{\epsilon}) = \frac{1}{\pi v^{*2}}\exp[-\frac{\epsilon^2+\bar{\epsilon}^2}{v^{*2}}]$ is the joint density of states.

D. Generalized tunneling formula for the current in NESSs

Here we introduce a tunneling formula for the current in NESSs and simplified versions of it. A more detailed derivation can be found in Appendix A. For the derivation, we choose one direction in the hypercubic lattice (let us say x) and regard the system as a stack of $(d-1)$-dimensional slabs, which are aligned in the x direction. The bias is applied to the x direction and each slab is connected to the neighboring slab by l^{d-1} (with $l \to \infty$) tunneling junctions. The Hamiltonian can now be expressed as $\hat{H}(t) = \hat{H}_{\perp}(t) + \hat{V}_x(t)$, where $\hat{V}_x(t)$ describes the transfer integrals along the x direction (junctions between slabs), and $\hat{H}_{\perp}(t)$ describes the $(d-1)$-dimensional slabs. In order to prepare the NESS of the full system, we start from the Floquet steady state of decoupled slabs ($V_x = 0$), and switch on V_x adiabatically. We consider the effect of V_x in linear response and evaluate the current along the x direction (through the junctions between the slabs) considering that the steady states of the $(d-1)$-dimensional slabs can be approximated by those of the full d-dimensional bulk when d is large. Then we obtain the following expression of the current per site:

$$j_{\rm tun,mom}(t) = -qv^{*2}\int d\epsilon d\bar{\epsilon}\rho(\epsilon,\bar{\epsilon})\int_{-\infty}^{t} d\bar{t} \times \mathrm{Re}[G^{<}_{\epsilon,\bar{\epsilon}}(\bar{t},t)G^{>}_{\epsilon,\bar{\epsilon}}(t,\bar{t}) - G^{>}_{\epsilon,\bar{\epsilon}}(\bar{t},t)G^{<}_{\epsilon,\bar{\epsilon}}(t,\bar{t})]e^{-i\int_{\bar{t}}^{t}dt'E(t')}. \quad (18)$$

We note that this expression includes processes where an electron goes through a certain junction and returns to the original slab through a different junction; see Appendix A. It is also interesting to point out that by approximating $\epsilon^2 = \bar{\epsilon}^2 \simeq v^{*2}/2 = \int d\epsilon d\bar{\epsilon}\rho(\epsilon,\bar{\epsilon})\epsilon^2$ and $\epsilon\bar{\epsilon} \simeq 0 = \int d\epsilon d\bar{\epsilon}\rho(\epsilon,\bar{\epsilon})\epsilon\bar{\epsilon}$, Eq. (16) becomes Eq. (18).

By only considering the contribution to the current at a certain junction by electrons that went through the same junction, we obtain the generalized tunneling formula,

$$j_{\rm tun}(t) = -qv^{*2}\mathrm{Re}\Big[\int_{-\infty}^{t} d\bar{t}\{G^{<}_{\rm loc}(\bar{t},t)G^{>}_{\rm loc}(t,\bar{t}) - G^{>}_{\rm loc}(\bar{t},t)G^{<}_{\rm loc}(t,\bar{t})\}e^{-i\int_{\bar{t}}^{t}dt'E(t')}\Big]. \quad (19)$$

This formula is applicable both to the dc field and the ac field case. In the following sections, we will show that the tunneling formula Eq. (19) works quantitatively very well in a wide parameter range, both in the dc and ac excitation regime. We will also show that the formula is useful to study the HHG in Mott insulators. These analyses indicate that, at least in the parameter range studied in the paper, the neglected processes are not important. We also note that the expressions Eqs. (16), (18), and (19) are reminiscent of the Meir-Wingreen formula that is often used in the study of quantum dot and transport problems [48].

In the special case of NESSs driven by a dc field, using $G^{<>}_{\rm loc}(t,t') = G^{<>}_{\rm loc}(t-t')$ and $E(t) = E_0$, Eq. (19) can be expressed as

$$j_{\rm tun}(E_0) = qv^{*2}\pi\int_{-\infty}^{\infty} d\omega A_{\rm loc}(\omega)A_{\rm loc}(\omega+E_0) \times [f_{\rm loc}(\omega)(1-f_{\rm loc}(\omega+E_0)) - f_{\rm loc}(\omega+E_0)(1-f_{\rm loc}(\omega))]. \quad (20)$$

Here we note that $G(t,t') = G(t-t')$ is satisfied only by the local Green's function because the lattice Hamiltonian is time dependent in the temporal gauge. The general (gauge-dependent) Green's functions are not time-translation invariant. The same formula for dc-driven systems has been derived in Ref. [35] based on an expansion in v^*. In the present work, we provide a different derivation and generalize the formula to the ac regime [Eq. (19)].

Next we introduce some simplified versions of Eq. (19), which are inspired by naive expectations. In the ac case, $G^{<,>}_{\rm loc}(t_r;t_{\rm av})$ in general depends on $t_{\rm av}$ and $G^{<,>}_{\rm loc}(t,t') \neq G^{<,>}_{\rm loc}(t-t')$. In other words, there are contributions from the off-diagonal terms of $G_{\rm loc}$ in the Floquet representation and Eq. (19) cannot be expressed only with $t_{\rm av}$-averaged quantities. Still it is an interesting question how well the current is approximated by $t_{\rm av}$-averaged quantities. To investigate this issue, we introduce a simplified version of Eq. (19) by replacing $G^{<,>}_{\rm loc}(t,t')$ by $\bar{G}^{<,>}_{\rm loc}(t-t')$, where the bar indicates averaging over $t_{\rm av}$. We then approximate the current as

$$j_{\rm tun,av}(t) = -qv^{*2}{\rm Re}\Bigg[\int_0^\infty d\bar{t}\{\bar{G}^<_{\rm loc}(-\bar{t})\bar{G}^>_{\rm loc}(\bar{t}) - \bar{G}^>_{\rm loc}(-\bar{t})\bar{G}^<_{\rm loc}(\bar{t})\}e^{-i\int_{t-\bar{t}}^t dt' E(t')}\Bigg]. \quad (21)$$

Furthermore, one may consider a scenario where the current originates from tunneling induced by a quasistatic field between the Floquet states of two slabs. This picture can be tested by assuming that $E(t')$ is slowly (adiabatically) changing so that for the current at time t the field $E(t')$ in the integral can be replaced by $E(t)$. This leads to the approximation

$$j_{\rm tun,adi}(t) = -qv^{*2}{\rm Re}\Bigg[\int_{-\infty}^t d\bar{t}\{G^<_{\rm loc}(\bar{t},t)G^>_{\rm loc}(t,\bar{t}) - G^>_{\rm loc}(\bar{t},t)G^<_{\rm loc}(t,\bar{t})\}e^{-i(t-\bar{t})E(t)}\Bigg]. \quad (22)$$

Finally, one may combine the above two assumptions (time-average of the Green's function and the adiabaticity of the field) to obtain

$$\begin{aligned} j_{\rm tun,av,adi}(t) &= -qv^{*2}{\rm Re}\Bigg[\int_0^\infty d\bar{t}\{\bar{G}^<_{\rm loc}(-\bar{t})\bar{G}^>_{\rm loc}(\bar{t}) - \bar{G}^>_{\rm loc}(-\bar{t})\bar{G}^<_{\rm loc}(\bar{t})\}e^{-i\bar{t}E(t)}\Bigg] \\ &= qv^{*2}\pi\int_{-\infty}^\infty d\omega \bar{A}_{\rm loc}(\omega)\bar{A}_{\rm loc}(\omega+E(t)) \\ &\quad\times[\bar{f}_{\rm loc}(\omega)(1-\bar{f}_{\rm loc}(\omega+E(t))) \\ &\quad - \bar{f}_{\rm loc}(\omega+E(t))(1-\bar{f}_{\rm loc}(\omega))]. \end{aligned} \quad (23)$$

This formula captures the tunneling induced by the quasistatic field between the Floquet bands (photodressed states) appearing in the time-averaged spectrum.

At this point, let us emphasize that Eq. (19) is not an exact formula. One can show this by considering the linear response against $E(t)$. By expanding Eq. (19) in terms of $E(t)$, we find that the real part of the optical conductivity is given by

$${\rm Re}\sigma(\Omega) = \frac{qv^{*2}\pi}{\Omega}\int_{-\infty}^\infty d\omega A_{\rm loc,eq}(\omega)A_{\rm loc,eq}(\omega+\Omega) \times[f_{\rm eq}(\omega) - f_{\rm eq}(\omega+\Omega)]. \quad (24)$$

Here we used the fact that the inversion symmetry leads to the absence of a linear component in $E(t)$ in $G_{\rm loc}$ and the subscript "eq" indicates equilibrium quantities. On the other hand, the correct expression involves convolutions at each momentum, with momentum-dependent single-particle Green's functions [47]. One can show that Eq. (18) provides the exact expression of the linear optical conductivity.

As is shown in the following, the generalized tunneling formula works quantitatively well for the case of a hypercubic lattice in infinite spatial dimensions and provides important insights into the physical processes governing the current in the electric-field-driven system. The derivation of this formula, however, cannot fully justify its use in finite dimensions. Still, in finite-dimensional systems, we may regard the formula and the underlying ideas as a lowest-order approximation against the spatial dimensions ($1/d$ expansion), which should be useful to discuss physical processes and the role of dimensionality.

III. DC-FIELD-DRIVEN STEADY STATES

First, we discuss the effects of dc fields. When the applied field is strong enough, doublons and holons are created by tunneling processes and the Mott insulating phase becomes unstable. This phenomenon is called dielectric breakdown and the time evolution after switching on the field has been studied with exact diagonalization, time-dependent density matrix renormalization group, and DMFT calculations [11,13,22]. In the present study, we are interested in the properties of the NESSs that are reached after the transient dynamics in the presence of $H_{\rm bath}$.

A. Spectral function and occupation

First, we discuss the spectral function and the occupation in the NESS. In Fig. 2, we show the local spectral function [Figs. 2(a) and 2(b)], their occupancy [Figs. 2(c) and 2(d)], and the distribution function [Figs. 2(e) and 2(f)]. Without the field, the lower and upper Hubbard bands are located around $\omega = \pm U/2$, and their band width is about $2v^*$. As we increase the field strength, the width of the main Hubbard bands is reduced, which indicates that injected charge carriers are more localized. The local Green's function measures the probability for an added test charge to stay on the same site, and the bands in its spectrum become narrower when the charge cannot move around. Strong fields create a large potential energy difference between different sites, which suppresses the hopping and localizes the charge. This picture applies both to free electron systems [34] and to the present case of a Mott insulator, where the injected charges (doublons and holons) move in a random spin background [26,49].

In addition to this, under the dc field, Wannier-Stark states emerge from both the lower and upper Hubbard bands ($\omega_{{\rm ws},\pm,m} \simeq \pm U/2 + mE_0$). For $E_0 \gtrsim U/2$, other peaks that scale as $\omega_{{\rm ws2},\pm,\mp2} = \pm\frac{3}{2}U \mp 2E$ start to become prominent; see Figs. 2(a) and 2(b). The sideband $\omega_{{\rm ws2},+,-2} = \frac{3}{2}U - 2E_0$ represents a process where the insertion of one electron at a given site leads to the creation of a doublon and the simultaneous creation of another doublon-holon pair. This doublon-holon creation process costs an interaction energy of $\frac{3}{2}U$ (if the chemical potential contribution is subtracted). If

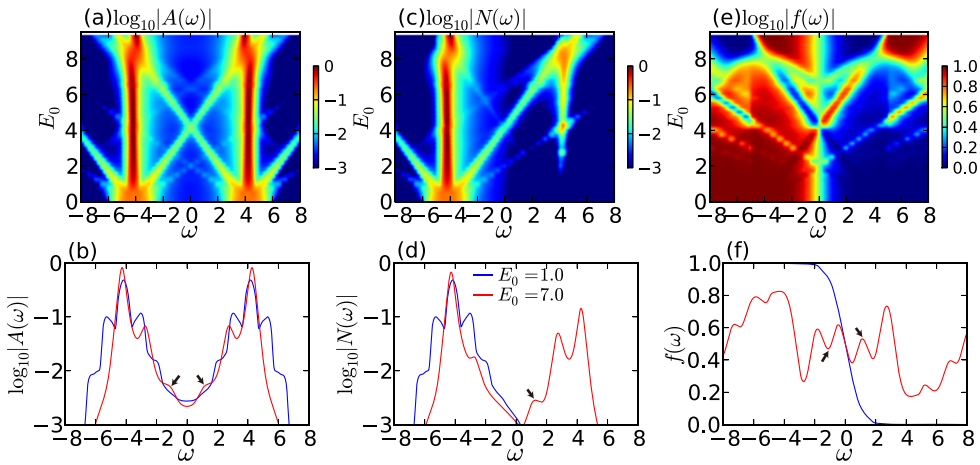

FIG. 2. [(a), (b)] The local spectral function $A(\omega)$, [(c), (d)] the occupation function $N(\omega)$, and [(e), (f)] the distribution function $f(\omega)$ of the Hubbard model with dc fields. In panels (b),(d),(f) we show cuts at $E_0 = 1$ and 7 to highlight the features discussed in the text. The structures indicated by arrows correspond to the Wannier-Stark states at $\omega_{\mathrm{ws2},\pm,\mp2} = \pm\frac{3}{2}U \mp 2E$. The parameters are $U = 8.0, \beta = 2.0, \Gamma = 0.06, W_{\mathrm{bath}} = 5.0$.

the separation between the additional doublon and holon in the field direction is two lattice spacings, there is a potential energy gain of $2E_0$. Without this energy gain from the field, the considered process is strongly suppressed and only produces a weak shoulder in the local spectral function at $\omega = \pm\frac{3}{2}U$, but our simulations show that it becomes relevant for $E_0 \gtrsim U/2$. There is also a very weak feature that follows $\omega_{\mathrm{ws2},\pm,\mp1} = \pm\frac{3}{2}U \mp E_0$ (only visible in a second derivative plot of the local spectral function). It corresponds to the process of creation of one doublon (holon) at a given site and the simultaneous creation (annihilation) of another doublon-holon pair with a separation of one lattice spacing in the field direction. The satellites at $\omega = \pm\frac{3}{2}U$ and the sidebands emerging from them are the result of electronic correlations. In a semiconductor model, these structures at $\omega_{\mathrm{ws2},\pm,\mp2} = \pm\frac{3}{2}U \mp 2E_0$ are absent; see Appendix B. By increasing the field, we observe a crossing of the main Hubbard bands ($\omega_{0,\pm} \simeq \pm\frac{U}{2}$) and the first Wannier-Stark states ($\omega_{\mathrm{ws},\pm,\mp1} \simeq \pm\frac{U}{2} \mp E_0$) around $E_0 \simeq U$. The spectrum in Fig. 2(a) shows that there occurs a hybridization between the main band and the Wannier-Stark state, which increases the splitting between the main bands ($|\omega_{0,+} - \omega_{0,-}|$) for $E_0 \lesssim U$ and deceases it for $E_0 \gtrsim U$.

We note that our results from FDMFT implemented with the NCA solver predict different properties of the spectral function around $E_0 = U/2$ from those obtained in Ref. [35]. In the latter work, FDMFT was implemented with an iterated perturbation theory (IPT) impurity solver and a Markovian quantum master equation was used to describe the effect of a bosonic thermal bath. This calculation produced Wannier-Stark states emerging from the field-induced midgap states at $E_0 = U/2$, but did not exhibit the peaks at $\omega = \pm\frac{3}{2}U \mp 2E_0$. The origin of these discrepancies remains unclear.

Now we turn to the occupation [$N(\omega)$] and the distribution function [$f(\omega)$]. The Wannier-Stark bands emerging from the lower Hubbard band and its satellite at $-\frac{3}{2}U$ are well occupied and prominently visible in $N(\omega)$; see Figs. 2(c) and 2(d). There are also maxima along these bands in $f(\omega)$; see Figs. 2(e) and 2(f). On the other hand, the Wannier-Stark bands emerging from $\omega > 0$ are less occupied and there are valleys (local minima) along these lines in $f(\omega)$; see Figs. 2(e) and 2(f). Still, a clear occupation of $\omega_{\mathrm{ws},+,-1}$ appears for $E_0 \gtrsim \frac{U}{2}$, which corresponds to the annihilation of an already existing doublon by the removal of an electron. For $E_0 \gtrsim \frac{U}{2}$, there already exist many doublons in the NESS because of the activated tunneling processes.

B. Current and double occupation

Now we move on to the double occupancy (d) and the induced dc current (j_{dc}); see Fig. 3. Both in d and j_{dc}, one can

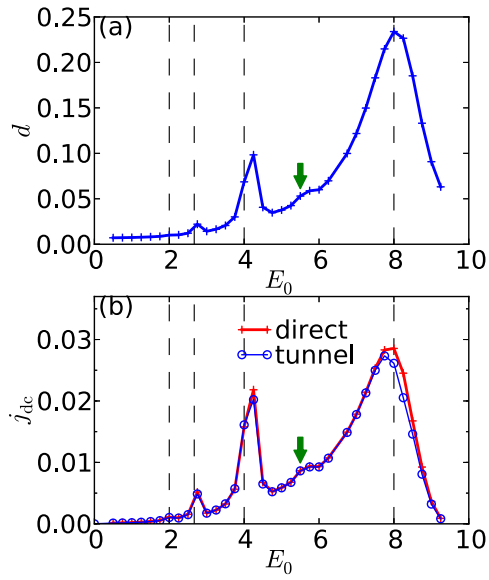

FIG. 3. [(a), (b)] Field-strength dependence of the double occupancy (d) and the current (j_{dc}) of the Hubbard model with dc field. In panel (b), the measured current is shown with red cross marks, while the current estimated by the tunneling formula, Eq. (20), is shown with blue circles. Vertical lines indicate $E_0 = U$, $U/2$, $U/3$, and $U/4$, and the arrows indicate humps at $E_0 \simeq 5.5 \simeq \frac{2}{3}U$. Here, $U = 8.0$, $\beta = 2.0$, $\Gamma = 0.06$, and $W_{\mathrm{bath}} = 5.0$.

observe clear peaks at $E_0 = U, U/2$, and $U/3$ and a small peak at $E_0 = U/4$. At $E_0 = U/m$, the excess potential energy from tunneling of an electron by m sites exactly compensates the energy required for the creation of a doublon-holon pair. Hence the doublon-holon pairs with a separation of m lattice spacings are resonantly created and enhance the double occupancy and the current. We also note that there is a hump around $E_0 \simeq 5.5 \simeq \frac{2}{3}U$ both in d and $j_{\rm dc}$. This feature corresponds to the simultaneous creation of two doublon-holon pairs, one with a separation of two lattice spacings and the other with a separation of one lattice spacing in the direction of the field. Again, such a resonance should be absent in the noninteracting case, which we have confirmed by analyzing a semiconductor model; see Appendix B.

These interpretations of the peak-hump structures in d and $j_{\rm dc}$ can be corroborated by considering the tunneling formula for the dc current, Eq. (20), which associates these structures with Wannier-Stark sidebands and main Hubbard bands in the spectrum. The results of Eq. (20) match very well the directly evaluated current; see Fig. 3(b). Using the tunneling formula, the $E_0 = U/3$ peak, for example, can be explained as follows: For this field strength, the spectral function exhibits clear peaks at (i) $-\frac{U}{2} = \omega_{{\rm ws},-,0}$, (ii) $-\frac{U}{2} + \frac{U}{3} = \omega_{{\rm ws},-,1} = \omega_{{\rm ws},+,-2}$, (iii) $\frac{U}{2} - \frac{U}{3} = \omega_{{\rm ws},-,2} = \omega_{{\rm ws},+,-1}$, and (iv) $\frac{U}{2} = \omega_{{\rm ws},+,0}$, which are equally spaced by $\frac{U}{3}$. According to Eq. (20), these peaks are the origin of the peak in $j_{\rm tun}$ at $\Omega = U/3$. Even though in (ii) and (iii) two different WS states are mixed, we have to remember that $\omega_{{\rm ws},-}$ tends to be more occupied than $\omega_{{\rm ws},+}$. Therefore, the main contribution should come from (a) $\omega_{{\rm ws},-,0} \to \omega_{{\rm ws},+,-2}$, (b) $\omega_{{\rm ws},-,1} \to \omega_{{\rm ws},+,-1}$, and (c) $\omega_{{\rm ws},-,2} \to \omega_{{\rm ws},+,0}$. Altogether, these processes describe tunneling over three sites, because $\omega_{{\rm ws},\pm,m}$ corresponds to a doublon or holon mainly located at the $|m|$th neighbor of the site on which we measure the local Green's function. The tunneling formula also correctly reproduces the hump at $E_0 \simeq \frac{2}{3}U$. This can be attributed to the peaks at (i) $-\frac{U}{2} = \omega_{{\rm ws},-,0}$, (ii) $-\frac{U}{2} + \frac{U}{3} = \omega_{{\rm ws}2,-,2} = \omega_{{\rm ws},+,-1}$, (iii) $\frac{U}{2} - \frac{U}{3} = \omega_{{\rm ws},-,1} = \omega_{{\rm ws}2,+,-2}$, and (iv) $\frac{U}{2} = \omega_{{\rm ws},+,0}$, which are equally spaced by $\frac{U}{3}$. The tunneling from (i) to (iii) and (ii) to (iv) is the origin of the hump at $E_0 \simeq \frac{2}{3}U$, which is associated with the creation of two doublon-holon pairs, as mentioned above.

IV. AC-FIELD-DRIVEN STEADY STATES

Next we discuss the effects of ac fields by considering various sets of parameters for the excitation frequency Ω and the field strength E_0. In particular, we are interested in the properties of NESSs in the crossover regime ($v^* \lesssim \Omega, E_0$), where the intuition gained from the dc limit and the weak-field ac limit may not be applicable anymore and the two pictures are expected to be mixed up.

A. Spectral function and occupation

In Fig. 4, we summarize the time-averaged local spectral functions $\bar{A}_{\rm loc}(\omega)$ and time-averaged occupancies $\bar{N}_{\rm loc}(\omega)$ for $\Omega = 0.5, 1.0, 1.5, 2.0, 3.0, 4.0, 6.0, 8.0 \leqslant U$ and $E_0 \leqslant U$. Here we note that $\Omega = 0.5, 1.0, 2.0, 4.0, 8.0$ satisfy the resonance condition $n\Omega = U$. In the spectrum, when Ω is small ($\lesssim v^* = 1.0$), one can still identify side peaks around the Hubbard bands that scale linearly with E_0; see red circles for $\Omega = 0.5$. These correspond to the Wannier-Stark states in the dc limit. As we increase the excitation frequency, we enter a crossover regime. There, in addition to the Wannier-Stark ladders, one starts to observe clear features at $\pm\frac{U}{2} + m\Omega$, which are reminiscent of the Floquet side bands of the Hubbard bands expected in the high-frequency regime; see, for example, $\Omega = 1.5$. As we further increase the excitation frequency, the Wannier-Stark-like features become less prominent and one can only observe the Floquet side bands of the Hubbard bands at $\pm\frac{U}{2} + m\Omega$; see white circles for $\Omega = 2.0$, for example. In general, the width of the main bands is reduced in the presence of the field, compared to the equilibrium value, and it changes as a function of the field strength. The reduction of the band under strong fields indicates that the injected charge carriers are more localized, just as in the dc case [34,50–52]. However, since the ac field is oscillating, a larger field amplitude is required to produce the same effects. The minimum width is observed when $J_0(E_0/\Omega) = 0$ as in the free electron case (see below), where J_0 is the zeroth Bessel function. The Floquet side bands become also very prominent here. To clearly reveal this dependence, we plot $\bar{A}_{\rm loc}(\omega)$ as a function of the strength of the vector field, $A_0 = E_0/\Omega$; see the right row of Fig. 4. A minimum is around $A_0 = 2.4$, which is close to the first zero crossing of the Bessel function $J_0(A_0)$. We also note that the renormalization and hence the minimum is less prominent for $\Omega = 4.0, 8.0$. This appears to be because the hybridization of the Floquet side bands of the lower and upper Hubbard band widens the band. The same should happen at $\Omega = 2.0$ but the weights of the Floquet side bands are small compared to the other cases, so that this effect is not prominent.

It is instructive to compare the spectra of the driven Mott insulators with those of driven free electron systems [34]. For the hypercubic lattice and the electric field pointing in the body-diagonal direction, the free electron spectral function is

$$\bar{A}_{\epsilon,\bar{\epsilon}}(\omega) = \sum_m \delta(\omega - m\Omega - \epsilon J_0(A_0)) \times \left| \int_0^{2\pi} \frac{dx}{2\pi} e^{imx} \exp\left[-\frac{i}{\Omega} \int_0^x dz \epsilon [\cos(A_0 \sin z) - J_0(A_0)] + \bar{\epsilon} \sin(A_0 \sin z) \right] \right|^2, \quad (25)$$

where the momentum information is again encoded in $\epsilon = -2v \sum_{i=1}^d \cos(k_i)$ and $\bar{\epsilon} = -2v \sum_{i=1}^d \sin(k_i)$. From this, one can see that at each momentum the spectrum shows peaks at $\epsilon J_0(A_0) + m\Omega$. The time-averaged local spectrum is expressed as $\bar{A}_{\rm loc}(\omega) = \int d\epsilon d\bar{\epsilon} \rho(\epsilon,\bar{\epsilon}) \bar{A}_{\epsilon,\bar{\epsilon}}(\omega)$, where $\rho(\epsilon,\bar{\epsilon}) = \frac{1}{\pi v^{*2}} \exp[-\frac{\epsilon^2+\bar{\epsilon}^2}{v^{*2}}]$ is the joint density of states. In the left row of Fig. 4, we show the time-averaged local spectrum for the free electrons. One can easily recognize the similarity between the free electron spectrum and the upper and lower Hubbard bands of the Mott insulator under the periodic driving. Namely, for small Ω compared to the band width $\simeq 2v^*$, structures resembling the WS ladders can be still identified; see the red circle for $\Omega = 0.5$. For higher frequencies, one can observe clear Floquet side bands around $\omega = n\Omega$; see the white circle for $\Omega = 2.0$, for example. When $J_0(A_0) = 0$, the position of

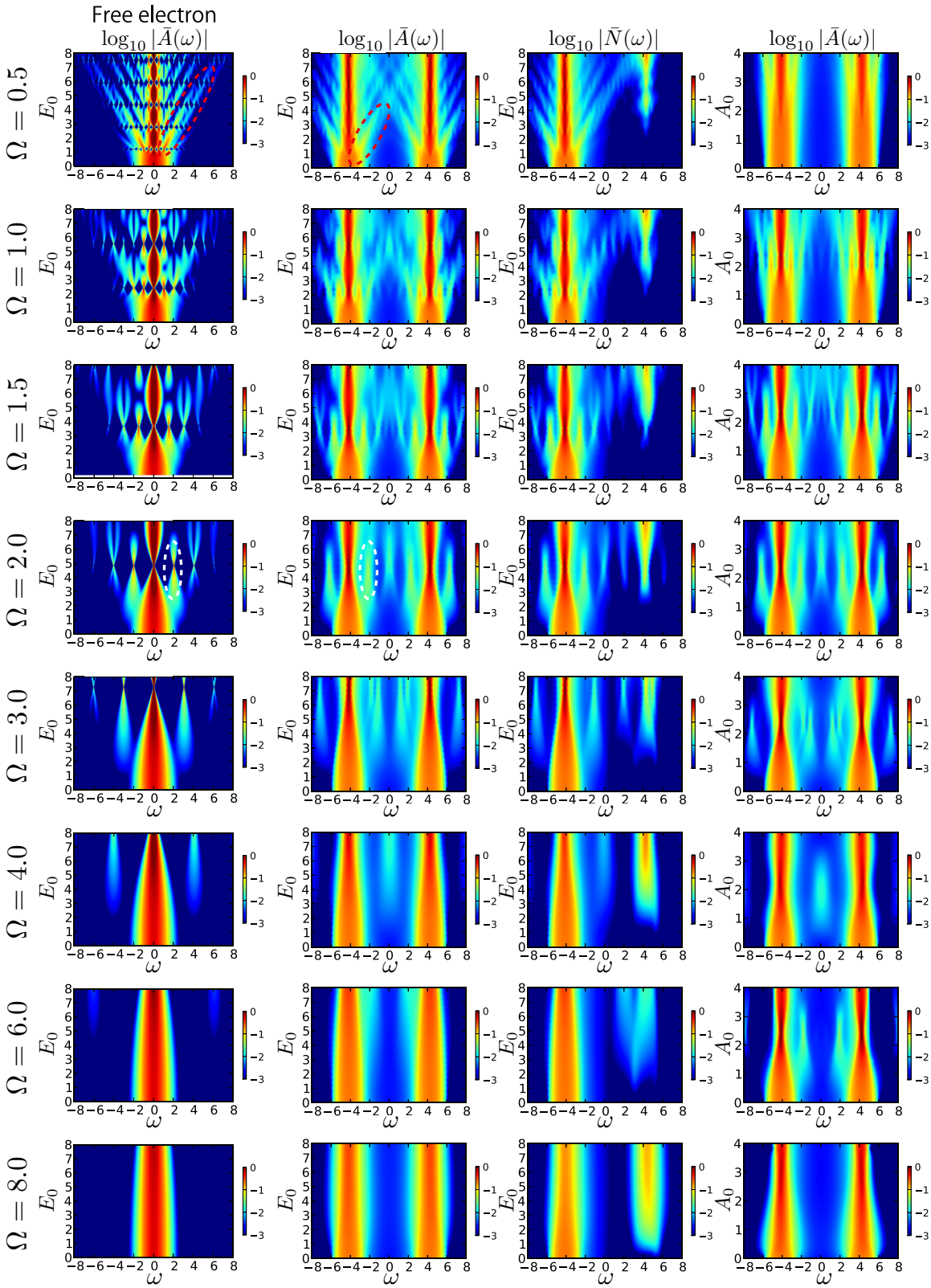

FIG. 4. Log-scale plots of the time-averaged local spectral function $\bar{A}(\omega)$ and time-averaged local occupation function $\bar{N}(\omega)$ of the Hubbard model driven by ac fields with indicated frequencies Ω and amplitudes E_0. In the first column, the local spectral function for the free system ($U = 0$) is provided for comparison. In the second and third columns, the local spectral function and the occupation function are shown for the field-driven Mott insulating state, respectively. In the fourth column, the local spectral function is plotted against $A_0(= E_0/\Omega)$ instead of E_0, to illustrate the relation between the band narrowing and the zeroth-order Bessel function, $J_0(A_0)$. The red dotted circles in the figures for $\Omega = 0.5$ highlight a structure reminiscent of a WS state in the dc limit. The white circles in the figures for $\Omega = 2.0$ show a Floquet sideband of the main band. Here $U = 8.0, \beta = 2.0, \Gamma = 0.06, W_{\text{bath}} = 5.0$.

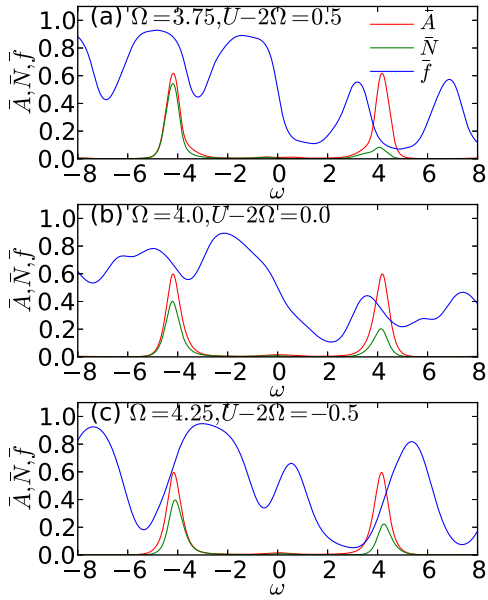

FIG. 5. [(a)–(c)] Time-averaged local spectrum, occupation, and distribution function around $\Omega = U/2$. The field strength is $E_0/\Omega = 1.841$. Here, $U = 8.0, \beta = 2.0, \Gamma = 0.06, W_{\text{bath}} = 5.0$.

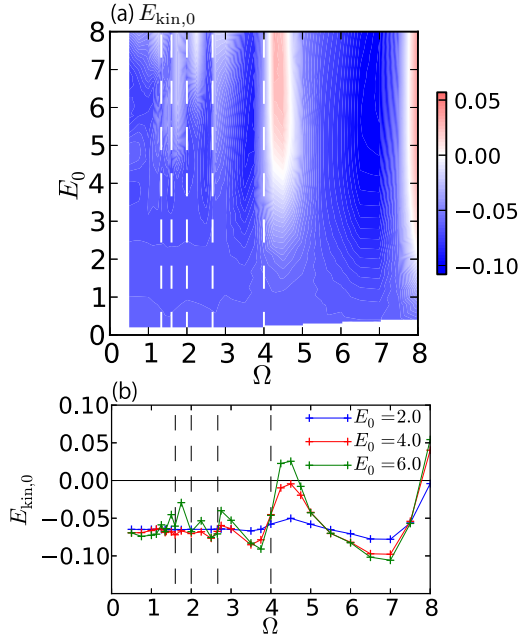

FIG. 6. (a) Time-averaged kinetic energy ($E_{\text{kin},0}$) in the plane of E_0 and Ω. In the red regime $E_{\text{kin},0}$ is positive, which cannot be realized in equilibrium and reflects the inverted population at $\Omega \gtrsim U/n$. (b) The dependence of $E_{\text{kin},0}$ on Ω for fixed E_0. The vertical lines show resonant points $\Omega = U/n$. Here, $U = 8.0, \beta = 2.0, \Gamma = 0.06, W_{\text{bath}} = 5.0$.

the peaks is at $n\Omega$ regardless of the momentum and this leads to clear Floquet side bands.

As in the dc case, the side peaks originating from the lower Hubbard bands tend to be more occupied compared to those originating from the upper Hubbard bands. The occupation of the upper Hubbard bands becomes prominent around $E_0 = U/2$ for small excitation frequencies Ω. This indicates that in this regime the tunneling picture of the dc limit still works and the creation of doublon-holon pairs on the next nearest neighbor site is activated at $E_0 = U/2$. At higher frequencies, the main upper Hubbard band starts to get occupied for smaller values of E_0, which indicates that in this regime, the doublons are not created by tunneling but rather by multiphoton processes.

We now discuss the similarities and differences between the NESSs and the Floquet prethermal states of isolated systems, which were recently discussed in Ref. [27]. In Figs. 5(a)–5(c), we show spectral functions, occupation functions, and distribution functions for $E_0/\Omega = 1.841$ around $\Omega = U/2$, where $x = 1.841$ corresponds to the first crossing of the zeroth and second Bessel function, $J_0(x) = J_2(x)$. We note that when $\Omega = U/2$ and $J_0(E_0/\Omega) = J_2(E_0/\Omega)$, the leading-order effective Hamiltonian obtained from the high-frequency expansion becomes the free Hamiltonian [53]. In the previous study, we found that the Floquet prethermal state is characterized by (i) a periodic distribution function $\bar{f}(\omega)$, i.e., $\bar{f}(\omega) \simeq \bar{f}(\omega + \Omega)$ and (ii) an inverted population for $\Omega \gtrsim U/2$. The observation (i) can be well explained by regarding the Floquet prethermal state as a thermal state of the effective Hamiltonian.

Figure 5 shows that such a periodicity in $\bar{f}(\omega)$ is not observed in the NESS, even though there is some reminiscent structure. From this, it seems unlikely that the NESS can be described as an equilibrium state of some effective Hamiltonian derived from a high-frequency expansion. Still, for $\Omega \gtrsim U/2$ we can observe a population inversion in both the upper Hubbard band and the lower Hubbard band; i.e., the higher energy part of each band is more populated than the lower energy part; see Fig. 5(c). This is similar to Ref. [27] and to the inversion for $\Omega \gtrsim U$ in a periodically driven Falicov-Kimball model [40]. This inverted population indicates that there are more doublons and holons with high kinetic energy, which results in a positive time-averaged (total) kinetic energy $E_{\text{kin},0}$, as is shown in Figs. 6(a) and 6(b). We note that in equilibrium, $E_{\text{kin},0} \leqslant 0$. One can also observe a tendency of $E_{\text{kin},0}$ becoming positive around higher order resonances $\Omega = U/n$.

B. Current and double occupation

Now we move on to the behavior of the induced current $j(t) = \sum_n e^{in\Omega} j_n$ and the double occupation $d(t) = \sum_n e^{in\Omega} d_n$. These quantities oscillate periodically and they include the components of higher harmonics in terms of Ω. Because of the inversion symmetry of the system, $j(t)$ only includes odd harmonics, while $d(t)$ has even harmonics. In this section, we mainly focus on the lowest component, namely j_1 for the current and d_0 for the double occupancy. We discuss the higher order components at the end of this section and also in the following section, which focuses on high-harmonic generation.

The behavior of d_0 and j_1 in the dc limit and weak-field ac limit can be well understood in terms of tunneling and multiphoton absorption, respectively, but the values of these quantities at finite Ω and E_0 are difficult to predict. From the behavior in these limits, one may expect resonances at $E_0 = U/n$ and $\Omega = U/n$ to extend into the regions of finite

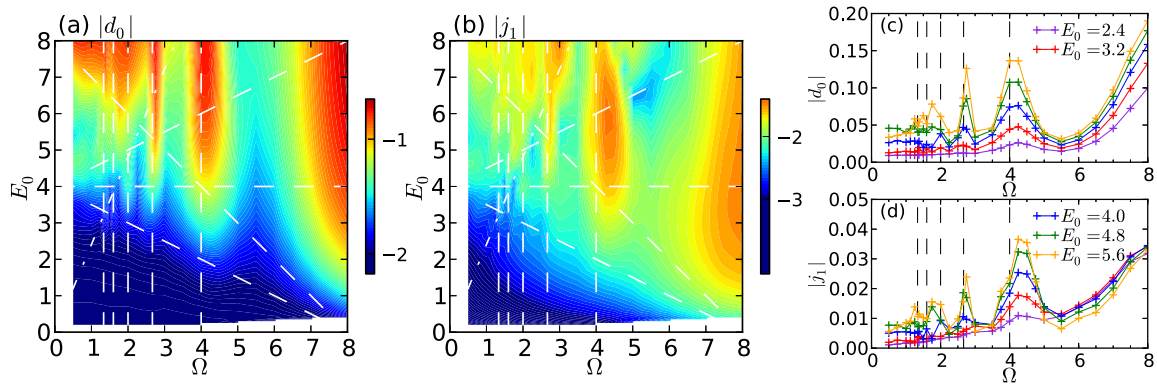

FIG. 7. [(a), (b)] Log-scale contour plot of the static component of the double occupancy (time-averaged, $|d_0|$) and the first-order harmonic component of the current ($|j_1|$) in the plane of the field strength E_0 and the excitation frequency Ω. The dashed lines show $\Omega = U/n$, $E_0 = U/2$, $U = E_0 + \Omega$, and $U = 2E_0 \pm \Omega$, where resonant excitations are expected. The dash-dotted line indicates $J_0(E_0/\Omega) = 0$. Resonant behaviors are found in $|d_0|$ and $|j_1|$ at $\Omega = U/n$ and they can be clearly seen around $E_0 \simeq U/2 = 4$. For low excitation frequencies ($\Omega \lesssim 1.0$), strong signatures of $|d_0|$ and $|j_1|$ are found around $E_0 = 4$, as in the dc limit, but they are slightly shifted to larger E_0 as Ω is increased. [(c), (d)] Cuts for fixed E_0. Here, $U = 8.0, \beta = 2.0, \Gamma = 0.06, W_{\text{bath}} = 5.0$.

frequency and significant field strength. Somewhere between these two limits, there occurs a crossover from the nonlinear transport regime (dc-like response) to the nonlinear optics regime (ac-like response). The corresponding crossover line, known as the *Keldysh line* [54], has been studied in 1D Mott insulators [17]. This crossover line should scale as $E_0 \propto \Omega$ with a slope that is determined by the characteristic doublon-holon separation (ξ). In addition, one could naively expect an interplay between tunneling and multiphoton absorption processes in the crossover regime ($v^* \lesssim \Omega, E_0$) such as field-induced tunneling between Floquet sidebands of the time-averaged spectral function. If such processes were relevant, one should detect noticeable changes in d_0 and j_1 along certain lines in the E_0-Ω plane. For example, the line $U = E_0 + \Omega$ would delimit the region in which doublon-holon creation by the combination of tunneling plus single-photon absorption becomes relevant, while the line $U = 2E_0 + \Omega$ corresponds to two tunnelings and a single-photon absorption.

In Figs. 7(a) and 7(b), we plot the numerical results of our Floquet-DMFT (NCA) simulations in the space of Ω and E_0, with the naively expected crossovers or resonances indicated by white dashed lines. We do not show the Keldysh line, since with DMFT for the hypercubic lattice it is difficult to estimate the correlation length ξ, but we indicate the line $J_0(E/\Omega) = 0$, which corresponds to complete localization (first zero crossing of the Bessel function) in the band renormalization picture. The actual behavior is obviously very complex and a detailed understanding of all the features in these plots is beyond the scope of this study. One can easily identify peaks along the $\Omega = U/n$ lines in both d_0 and j_1 with clear resonances up to $n = 6$, which are clearly visible around $E_0 = 4$. We plot curves for fixed field strength near $E_0 = U/2 = 4$ as a function of Ω in Figs. 7(c) and 7(d). The general tendency for $E_0 \lesssim U/2$, that higher order peaks become more prominent with larger E_0, is consistent with the expectation in the perturbative regime that such processes are proportional to $|E_0|^{2n}$ for d_0 and $|E_0|^{2n-1}$ for j_1. By increasing the field strength beyond $E_0 \approx U/2$, some higher order resonances ($n \geqslant 4$) disappear or emerge at off-resonant conditions. These shifts in the peak positions may originate from a strong mixing of tunneling and multiphoton processes.

Signatures of the dc resonances can be seen up to $\Omega \lesssim 1 = v^*$; see Figs. 7(a), 7(b), 8(a), and 8(b). Most prominently, one can observe a peak around $E_0 \simeq U/2$, which becomes less prominent with increasing Ω, but remains visible as a hump. This is consistent with our analysis of the spectral functions in Fig. 4, which showed that in this driving regime, the WS peaks still show up in the local spectrum. The position of this hump tends to gradually shift to larger values of E_0 with increasing Ω, and very roughly follows the line $U = 2E_0 - \Omega$; see the inset of Fig. 8(a). (The tendency is more clearly visible in d_0.) While this could be evidence for combined tunneling and photon emission, a simpler explanation of the shift is that in the ac regime, the average field strength is reduced, so that a larger E_0 is needed for a significant doublon-holon production. By further increasing the excitation frequency, we enter the

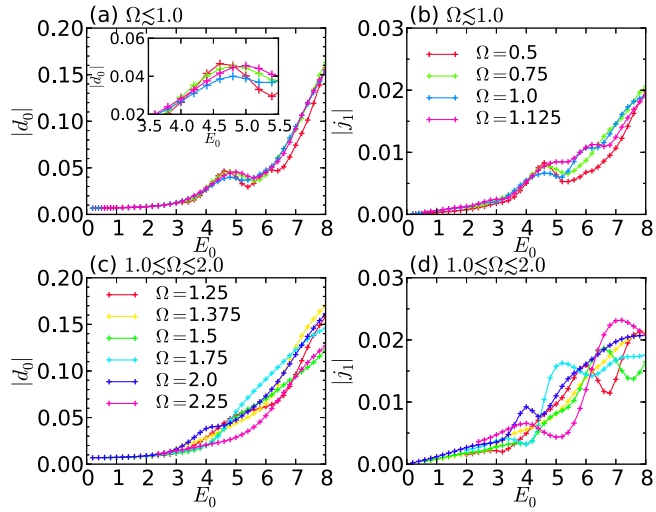

FIG. 8. E_0 dependence of d_0 and j_1 in the small-Ω regime. Here, $U = 8.0, \beta = 2.0, \Gamma = 0.06, W_{\text{bath}} = 5.0$.

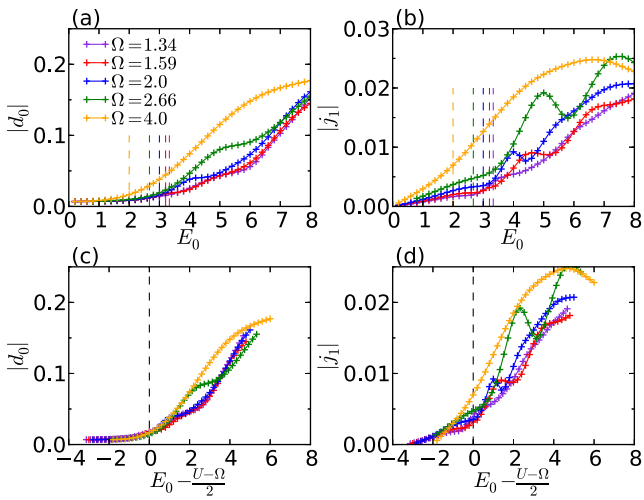

FIG. 9. E_0 dependence of d_0 and j_1 near the resonances $\Omega = U/n$. Panels (a) and (b) show the original data, and panels (c) and (d) show the results with the horizontal axis shifted by the "threshold field" $E_{0,\mathrm{line}} = (U-\Omega)/2$. Vertical lines indicate $E_{0,\mathrm{line}}$ for the parameters specified by the colors. Here, $U = 8.0, \beta = 2.0, \Gamma = 0.06, W_{\mathrm{bath}} = 5.0$.

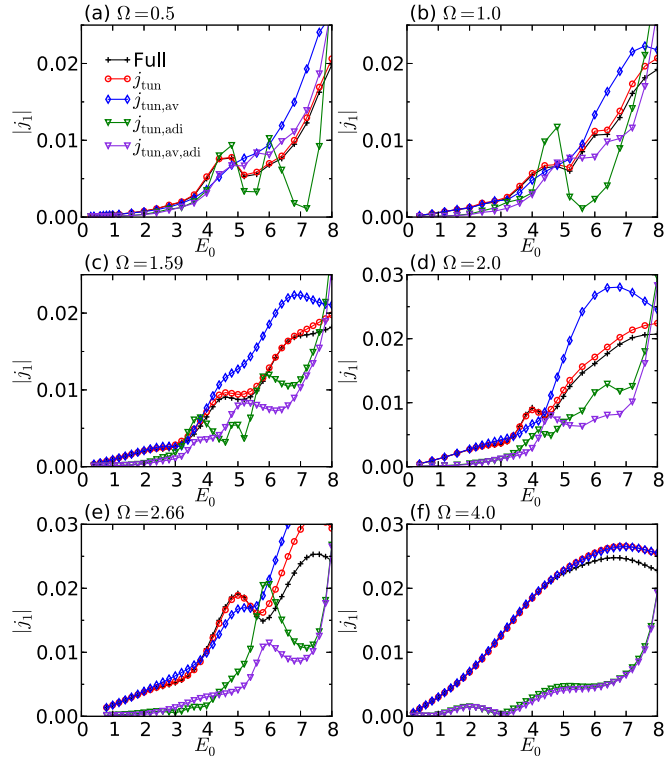

FIG. 10. Comparison of $|j_1|$ evaluated by different tunneling formulas for selected excitation frequencies near the resonances $n\Omega = U$. Here, $U = 8.0, \beta = 2.0, \Gamma = 0.06, W_{\mathrm{bath}} = 5.0$.

crossover regime, where the current and double occupancy show a very nontrivial dependence both on Ω and E_0; see Figs. 8(c) and 8(d).

At a first glance, the lines $U = E_0 + \Omega$, $U = 2E_0 + \Omega$, and $J_0(E/\Omega) = 0$ appear to be correlated with the structures revealed by the numerical simulations in the crossover regime. However, it is difficult to obtain conclusive evidence of processes involving tunneling between the Floquet sidebands. As an example, let us take a closer look at the $U = 2E_0 + \Omega$ line, which seems to correlate with an increase in d_0 and j_1. In Fig. 9, we plot the double occupation and the current (almost) at the resonances $\Omega = U/n$ as a function of E_0. The upper panels show the original data, while the lower panels plot these curves as a function of $E_0 - E_{0,\mathrm{line}}$, where $E_{0,\mathrm{line}} = \frac{U-\Omega}{2}$ is the "threshold value" predicted by the line $U = 2E_0 + \Omega$. This rescaling of the field strength roughly collapses the curves for the double occupation and the current. In particular, the upturn in the double occupation and current is roughly explained by $E_{0,\mathrm{line}}$, which may suggest an interplay between field-induced tunneling and photon absorption.

We can check to what extent the concept of tunneling between Floquet sidebands is meaningful by considering the tunneling formula for the current and its simplified versions. In particular, the approximation $j_{\mathrm{tun,av,adi}}$ defined in Eq. (23) is based on a picture of field-induced tunneling between the Floquet sidebands of the time-averaged spectral function.

Figure 10 compares the E_0 dependence of the current near the resonances $\Omega = U/n$ to the prediction of the tunneling formula and its approximations. First, we note that the full tunneling formula Eq. (19) is quantitatively accurate as long as the field is not too strong, and it is qualitatively good enough to capture the characteristic features of $|j_1|$. The simplified version Eq. (21) ($j_{\mathrm{tun,av}}$) based on t_{av}-averaged spectral functions can qualitatively reproduce almost all the characteristic structures except for the peak at $E_0 = 4$ and $\Omega = 2.0$. As expected, it becomes close to j_{tun} as Ω becomes larger. The current defined in Eq. (22) ($j_{\mathrm{tun,adi}}$), which is calculated under the assumption of adiabatically varying fields, is generally less accurate than j_{tun} and $j_{\mathrm{tun,av}}$. It can capture the behavior around $E_0 = 4 = U/2$ for small Ω, but it generally predicts complicated and unphysical structures. Still we note that for $\Omega = 0.5$, it is semiqualitatively good up to $E_0 = 5$, as expected from the adiabatic condition. The current $j_{\mathrm{tun,av,adi}}$ [Eq. (23)], which is calculated from t_{av}-averaged spectral functions under the assumption of adiabatically varying fields, is also less accurate than j_{tun} and $j_{\mathrm{tun,av}}$. Still it captures the peak structures around $E_0 = 4 = U/2$ at small Ω. We note that $j_{\mathrm{tun,av,adi}}$ does predict an upturn at roughly the expected value of $E_{0,\mathrm{line}} = (U-\Omega)/2$ (except for $\Omega = 4$), but significantly underestimates the current in the weak-field regime for $\Omega \gtrsim 1$. We thus conclude that while combined tunneling and multiphoton absorption processes may contribute to the structures in Fig. 7, a simple picture based on time-averaged Floquet spectral functions cannot fully capture the complexity of the nonequilibrium processes that govern the generic ac-driven system.

Now we move to see how well the induced current is described by a perturbative process. To this end, we evaluate the optical conductivities as

$$\sigma_n = j_n / E_0^{|n|}. \tag{26}$$

The lowest order contribution for the nth component current can be regarded as a process where the system absorbs n photons and generates a $n\Omega$ response, which scales as $E_0^{|n|}$.

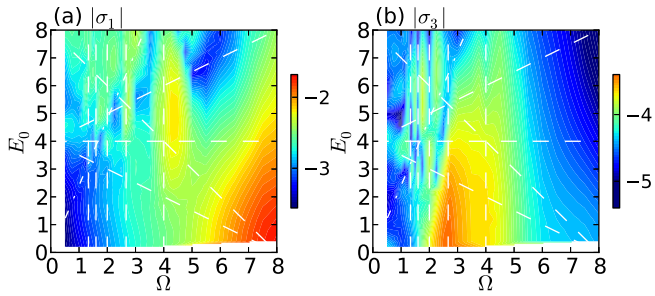

FIG. 11. [(a), (b)] Log-scale plot of the linear ($|\sigma_1|$) and third-order ($|\sigma_3|$) conductivity, which is defined in Eq. (26). In the weak-field regime, one can observe large values of $|\sigma_1|$ and $|\sigma_3|$ around $\Omega = U$ and $\Omega = U/3$, respectively. The latter resonance corresponds to three photon-absorption processes between the Hubbard bands. Here, $U = 8.0, \beta = 2.0, \Gamma = 0.06, W_{\rm bath} = 5.0$.

In Fig. 11, we show the results for $n = 1$ and 3. For $n = 1$, the conductivity is large around $U = 8$ in the weak-field regime. This is identical to the peak in the optical conductivity of the Mott state around $\omega = U$, which corresponds to the one-photon absorption process. For $n = 3$, there is a strong signal around $\Omega = U/3$ in the weak-field regime, which corresponds to the three-photon absorption process between Hubbard bands. As we increase the field strength, the system goes into the nonperturbative regime, and σ_n starts to exhibit a nonmonotonic behavior. One can identify peak structures at the resonances ($\Omega = U/n$) or between them, but in general it is difficult to identify the origin of these structures. Higher harmonic components in the current are related to high-harmonic generation (HHG), which we discuss in the next section.

C. High-harmonic generation and tunneling formula

In this section, we discuss how well the tunneling formulas can reproduce the higher order components of the current and hence HHG in Mott insulators. HHG originates from the strong interaction between light and matter [55–58]. Recently, it has been observed in semiconductors and the possibility of HHG in solids is attracting interest [59–79]. While most of the studies so far have focused on semiconductors, there has been some recent effort to extend this concept to strongly correlated systems [42,80,81].

In a separate study, Ref. [42], we investigated HHG in Mott insulators using FDMFT and the tunneling formula, which allowed us to distinguish the contributions from recombination and hopping of doublons and/or holons. Here we show complementary results which allow us to assess the accuracy of the tunneling formula and its simplified versions. In the present case, the HHG spectrum is given by $I_{\rm hh}(n\Omega) = |n\Omega j(n\Omega)|^2$ with $n \in \mathbb{Z}$ [64,75,80], which is proportional to the power radiated at the given frequency. This is because the acceleration of the charges generates electromagnetic field radiation.

In Ref. [42], it has been pointed out that the creation mechanism of HHG in the Mott state is different in the weak and strong field regimes. In Fig. 12, we show results representing these two regimes. In both regimes, the full tunneling formula Eq. (19) almost perfectly reproduces the

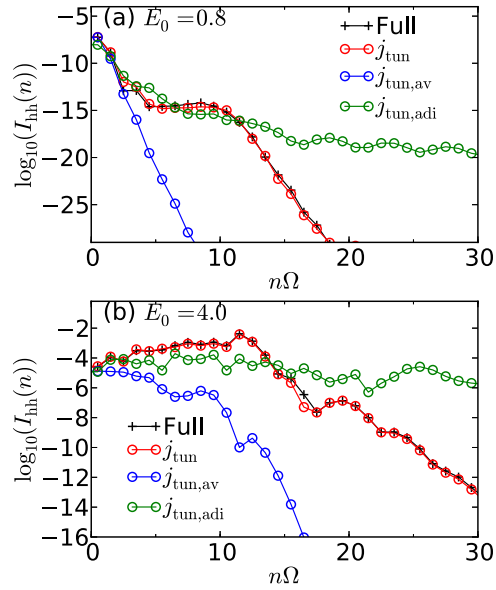

FIG. 12. Comparison of the high-harmonic-generation spectra evaluated by different tunneling formulas. Here, $U = 8.0, \beta = 2.0, \Gamma = 0.06, W_{\rm bath} = 5.0$.

exact result. This indicates that Eq. (19) is powerful enough to correctly predict the high-order components of the current. On the other hand, the simplified formulas based on the time-averaged Green's functions [$j_{\rm tun,av}$, Eq. (21)] and the adiabaticity of the field [$j_{\rm tun,adi}$, Eq. (22)] fail to reproduce the characteristic plateau structures. To be more precise, in the weak-field case, both $j_{\rm tun,av}$ and $j_{\rm tun,adi}$ roughly reproduce the results for the low-order harmonics, while in the strong field regime, only $j_{\rm tun,adi}$ roughly reproduces these results. On the other hand, both formulas fail to reproduce the higher order harmonics, including the plateaus. These results show that the HHG is the consequence of a nontrivial interplay between the nonadiabaticity of the field and the dependence of the Green's function on the average time.

D. Experimental relevance

Finally, we briefly comment on the experimental relevance of our results. In the dc case, the field strengths considered here ($qE_0a \sim U \sim e$V) may be difficult to achieve in reality. However, it is nowadays possible to produce few-cycle electric field pulses with $\sim$1 V/Å in the THz regime [60–63], which corresponds to $qE_0a \sim U \sim e$V. A comparison to the direct time evolution of the Hamiltonian Eq. (1) in the Kadanoff-Baym formalism [43] shows that a few field cycles are generally sufficient to almost reach a NESS, at least for the present choice of heat bath, whose coupling constant (Γ) is very small compared to the typical energy scales of the system. As an example, we plot in Fig. 13 the time evolution of the current after an ac field quench [$E(t) = E_0 \sin(\Omega t)$] at $t = 0$. Here, the system is in equilibrium at $t = 0$ and the excitation frequency is $\Omega = 0.5$, which is much smaller than U and the Mott gap. After a few cycles, the current approaches the steady-state solution evaluated from Floquet DMFT. This observation suggests that even though the simulated fields are

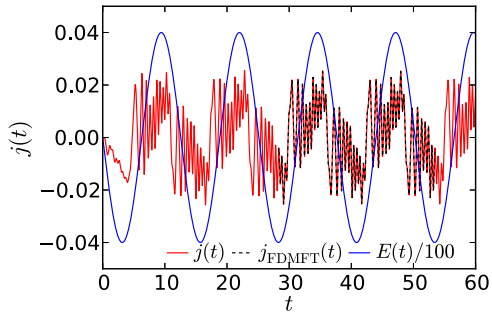

FIG. 13. Comparison between the time evolution of the current under an ac field quench at $t = 0$ and the current evaluated from Floquet DMFT. The applied field $[E(t) = E_0 \sin(\Omega t)]$ is also indicated. We use $\Omega = 0.5, E_0 = 4.0, U = 8.0, \beta = 2.0, \Gamma = 0.06, W_{\text{bath}} = 5.0$. The Floquet DMFT result is shifted by $9\pi/\Omega$ and $13\pi\Omega$.

rather strong, the ac-driving regime considered in our study can be accessed in experiments.

V. CONCLUSIONS

We systematically investigated the properties of the NESSs realized in large-gap Mott insulators driven by dc or ac electric fields. To this end, we applied the Floquet DMFT (implemented with an NCA impurity solver) to the Hubbard model coupled to a free electron bath. We also introduced a generalized tunneling formula [Eq. (19)] for the current, which resembles the Meir-Wingreen formula, as well as simplified versions neglecting the t_{av} dependence of the Green's functions or assuming an adiabatic evolution of the field. The full formula is derived by considering the tunneling between two neighboring slabs in Floquet steady states, and it provides a direct relation between the structures of the single-particle Green's function and the induced current. We also derived the exact expression of the current in DMFT [Eq. (16)] and pointed out the relations between the tunneling formulas.

First, we considered dc-driven systems and demonstrated the emergence of Wannier-Stark peaks from the lower and upper Hubbard bands in the spectrum. This result is consistent with the previous literature [25,26,50]. In addition, we revealed WS peaks originating from many-body processes, which are absent in semiconductors. These states can be connected to peaks and humps in the induced dc current through the tunneling formula.

Second, we studied the generic ac-driven system and thus shed light on the complicated crossover regime which connects the dc limit and the weak-field ac limit. When the excitation frequency Ω is small enough ($\Omega \lesssim v^*$), one can still identify the WS peaks in the time-averaged spectrum and the behavior of the current and double occupancy resembles the result for the dc case. In the crossover regime, i.e., when $v^* \lesssim \Omega, E_0$, the behavior of the current and the double occupation is in general very complicated. Characteristic resonance structures at $\Omega = U/n$ in the double occupation and the current can be observed when the field is strong enough but not too strong ($E_0 \lesssim U/2$). When the field becomes stronger ($E_0 \gtrsim U/2$), the higher n resonances start to be affected by tunneling processes, which leads to the suppression of peaks or shifts to nonresonant frequencies. Rough data collapses along certain lines (e.g., $U = 2E_0 + \Omega$) suggest a possible cooperative effect between tunneling and photon absorption, although an analysis based on the simplified tunneling formulas showed that the naive picture of tunneling between sidebands of the time-averaged Floquet spectra cannot fully capture the properties of the driven states. The full tunneling formula, on the other hand, works well in the generic ac case, and this may provide a basis for further analysis of the physical processes governing the crossover region.

We have also studied the vicinity of the regime where the effective static Hamiltonian obtained from a high-frequency expansion becomes a free Hamiltonian. In contrast to the Floquet prethermal states in isolated systems [27], the NESSs exhibit a time-averaged distribution function $\bar{f}(\omega)$ which is not periodic in ω (with period Ω). This indicates that the steady state cannot be described as an equilibrium state of the effective static Hamiltonian. Still, reflecting the inverted population of Floquet prethermal states, one can identify driving regimes where the kinetic energy is positive.

Finally, we discussed the ability of the tunneling formula and its simplified versions to describe the HHG spectrum of Mott insulators. The full tunneling formula is quantitatively good, while the simplified versions fail to capture the HHG features and the plateau structures in the HHG spectrum.

The manipulation of systems by continuous periodic excitations (so-called Floquet engineering [2,82–87]) is a promising strategy for the exploration of new properties or functionalities of materials. We hope that our systematic study of Floquet NESSs of Mott insulators, covering a wide range of excitation conditions, may serve as a reference point for further investigations of Floquet steady states in strongly correlated systems. In addition, the generalized tunneling formula is useful to obtain insights into the processes that contribute to the current in Floquet steady states. It would be an interesting future work to extend this approach to more complicated models including multiorbital and electron-phonon problems, in order to reveal the underlying physics.

ACKNOWLEDGMENTS

We thank M. Eckstein and M. Schüler for helpful discussion. This work was supported by the Swiss National Science Foundation through NCCR MARVEL and the European Research Council through ERC Consolidator Grant No. 724103. The calculations have been performed on the Beo04 cluster at the University of Fribourg and the CSCS Dora cluster provided by MARVEL.

APPENDIX A: DERIVATION OF THE TUNNELING FORMULA FOR NESSs

Here we introduce the generalized tunneling formula for the current in the nonequilibrium steady states (NESS), which helps us to understand physical processes involved. To derive the formula, we first select one direction in the hypercubic lattice (x) and regard the system as a stack of $(d-1)$-dimensional slabs, which are aligned in the x direction. The Hamiltonian

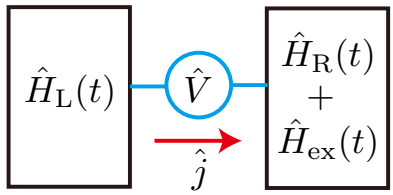

FIG. 14. Schematic picture of two subsystems in Floquet steady states, which are connected by junctions ($\hat{V}$).

can now be expressed as $\hat{H}(t) = \hat{H}_\perp(t) + \hat{V}_x(t)$ with

$$\hat{H}_\perp(t) = -\sum_{\langle i,j\rangle_\perp,\sigma} v_{ij}(t) c^\dagger_{i,\sigma} c_{j,\sigma} + U\sum_i n_{i\uparrow} n_{i\downarrow} + H_{\rm bath}, \tag{A1}$$

$$\hat{V}_x(t) = -\sum_{\langle i,j\rangle_\parallel,\sigma} v_{ij}(t) c^\dagger_{i,\sigma} c_{j,\sigma}. \tag{A2}$$

Here $\langle i,j\rangle_\perp$ indicates $\mathbf{r}_i - \mathbf{r}_j \perp \mathbf{e}_x$ and $\langle i,j\rangle_\parallel$ indicates $\mathbf{r}_i - \mathbf{r}_j \parallel \mathbf{e}_x$. In the Floquet steady state, the initial correlations should be washed out because of the heat bath. Therefore, one can prepare the steady states of the full system by starting from a steady state of $\hat{H}_\perp$, where all slabs are disconnected, and adiabatically switching on $\hat{V}_x$. When U is large, the effect of $\hat{V}_x$ may be treated perturbatively. Here we consider the linear contribution and evaluate the current in the x direction.

In this setup, in order to evaluate the current that flows between a pair of neighboring slabs, we only need to focus on these two neighboring slabs, because processes involving several slabs are coming from higher order processes in $\hat{V}_x$. We denote these slabs by L and R. After changing the gauge in the x direction to the scalar gauge, the bias is applied to the x direction and each slab is connected to the neighboring slab by l^{d-1} tunneling junctions. Here d is the spatial dimension; we consider l^d lattices and take the thermodynamic limit $l \to \infty$ in the end. The total Hamiltonian of these two slabs and the junctions between them can be written as $\hat{H}_{\rm tot}(t) = \hat{H}_{{\rm tot},0}(t) + \hat{V} = \hat{H}_{\rm L}(t) + \hat{H}_{\rm R}(t) + \hat{H}_{\rm ex}(t) + \hat{V}$ with

$$\begin{aligned}
\hat{H}_{\rm L}(t) &= \hat{H}_{\rm L}(t; c^\dagger_{L,i_\perp,\sigma}, c_{L,i_\perp,\sigma}),\\
\hat{H}_{\rm R}(t) &= \hat{H}_{\rm R}(t; c^\dagger_{R,i_\perp,\sigma}, c_{R,i_\perp,\sigma}),\\
\hat{H}_{\rm ex}(t) &= E(t)\sum_{i_\perp,\sigma} n_{R,i_\perp,\sigma},\\
\hat{V} &= -v\sum_{\sigma,i_\perp}[c^\dagger_{{\rm L},i_\perp,\sigma} c_{R,i_\perp,\sigma} + c^\dagger_{{\rm R},i_\perp,\sigma} c_{L,i_\perp,\sigma}].
\end{aligned} \tag{A3}$$

In Fig. 14, we illustrate this situation. Here $i_\perp$ is the site index perpendicular to x, and $\hat{H}_{\rm L,R}$ conserves the number of particles in the subsystems. We note that L and R are decoupled initially and the system is described by the time periodic Hamiltonian $\hat{H}_{{\rm tot},0}(t)$. Under the continuous driving, each slab is in a time-periodic steady state (Floquet steady state). Hence the initial wave function is one of the Floquet solutions of $\hat{H}_{{\rm tot},0}(t)$,

$$\left|\Psi^{(0)}_{{\rm tot},\alpha\beta}(t)\right\rangle_s = \left|\Psi^{(0)}_{{\rm L},\alpha}(t)\right\rangle_s \otimes \left|\Psi^{(0)}_{{\rm R},\beta}(t)\right\rangle_s e^{-i\int^t d\bar{t} E(\bar{t}) N_{R,\beta}}. \tag{A4}$$

Here the subscript "s" indicates the Schrödinger representation and $|\Psi^{(0)}_{X,\alpha}(t)\rangle_s$ is the Floquet solution of the time periodic Hamiltonian $\hat{H}_X$ ($X = {\rm R}, {\rm L}$), whose indices are α. $N_{{\rm R},\beta}$ is the number of particles in the right subsystem. We adiabatically switch on $\hat{V}$ from a certain time t_0 ($\to -\infty$), wait for a long time, and measure the induced current between the subsystems,

$$\hat{j} = iqv\sum_{\sigma,i_\perp,\sigma}[c^\dagger_{{\rm L},i_\perp,\sigma} c_{R,i_\perp,\sigma} - c^\dagger_{{\rm R},i_\perp,\sigma} c_{L,i_\perp,\sigma}]. \tag{A5}$$

The first-order correction of $\hat{V}$ to the state is

$$|\Psi_{{\rm tot},\alpha\beta}(t)\rangle_s \simeq \left|\Psi^{(0)}_{{\rm tot},\alpha\beta}(t)\right\rangle_s - i\int_{-\infty}^t d\bar{t}\hat{\mathcal{U}}_0(t,\bar{t})\hat{V}\left|\Psi^{(0)}_{{\rm tot},\alpha\beta}(\bar{t})\right\rangle_s. \tag{A6}$$

Here $\hat{\mathcal{U}}_0(t,t') = \mathcal{T}\exp[-i\int_{t'}^t d\bar{t}\hat{H}_{{\rm tot},0}(\bar{t})]$ for $t > t'$ and $\mathcal{T}$ is the normal time-ordering operator. From this, we obtain the current per junction

$$j(t) = -i\frac{1}{l^{d-1}}\int_{-\infty}^t d\bar{t} s\left\langle\Psi^{(0)}_{{\rm tot},\alpha\beta}(t)\right|\hat{j}\hat{\mathcal{U}}_0(t,\bar{t})\hat{V}\left|\Psi^{(0)}_{{\rm tot},\alpha\beta}(\bar{t})\right\rangle + {\rm H.c.} \tag{A7}$$

Here the zeroth-order term vanishes because of particle conservation. Using the facts that $|\Psi^{(0)}_{{\rm tot},\alpha\beta}(t)\rangle_s$ and $\hat{\mathcal{U}}_0(t,t')$ is the direct product of components of the left and right subsystems, we can derive the following form of the current:

$$\begin{aligned}
j(t) = -2qv^2\frac{1}{l^{d-1}}\sum_{i_\perp,j_\perp}\int_{-\infty}^t d\bar{t}\big\{&G^<_{{\rm L},\alpha,{\rm i}_\perp{\rm j}_\perp}(\bar{t},t)G^>_{{\rm R},\beta,{\rm j}_\perp{\rm i}_\perp}(t,\bar{t})\\
&- G^>_{{\rm L},\alpha,{\rm i}_\perp{\rm j}_\perp}(\bar{t},t)G^<_{{\rm R},\beta,{\rm j}_\perp{\rm i}_\perp}(t,\bar{t})\big\}e^{-i\int_{\bar{t}}^t dt' E(t')} + {\rm H.c.}
\end{aligned} \tag{A8}$$

Here the factor of two comes from the spin degrees of freedom and for $X = {\rm L,R}$ and $\gamma = \alpha,\beta$,

$$G^<_{X,\gamma,i_\perp j_\perp}(t',t) = i\left\langle\Psi^{(0)}_{X,\gamma}(t)\right|c^\dagger_{X,j_\perp}\mathcal{U}_{0X}(t,t')c_{X,i_\perp}\left|\Psi^{(0)}_{X,\gamma}(t')\right\rangle, \tag{A9a}$$

$$G^>_{X,\gamma,i_\perp j_\perp}(t,t') = -i\left\langle\Psi^{(0)}_{X,\gamma}(t)\right|c_{X,i_\perp}\mathcal{U}_{0X}(t,t')c^\dagger_{X,j_\perp}\left|\Psi^{(0)}_{X,\gamma}(t')\right\rangle. \tag{A9b}$$

So far we have assumed that initially the left and right subsystems are in certain Floquet states, respectively. In reality, the Floquet steady state should be a mixed state of all Floquet states, $\rho_X(t) = \sum_\gamma \rho_\gamma |\Psi^{(0)}_{X,\gamma}(t)\rangle\langle\Psi^{(0)}_{X,\gamma}(t)|$, and we should use this as the initial state. Here ρ_γ is some weight factor. The expression of the current is obtained by taking the average

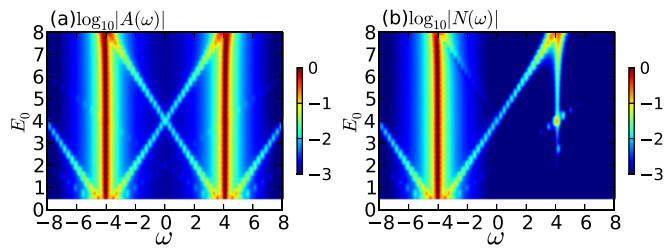

FIG. 15. (a) Local spectral function ($A(\omega)$) and (b) occupation function ($N(\omega)$) of the semiconductor model with a dc field. Here, $U = 8.0, \beta = 2.0, \Gamma = 0.06$.

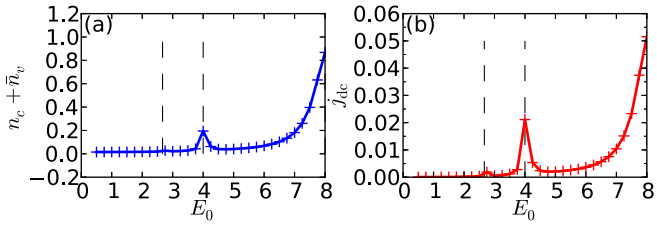

FIG. 16. [(a), (b)] Field-strength dependence of the number of charge carriers ($n_c + \bar{n}_v$), which corresponds to the double occupancy in the Mott insulators, and the current (j_{dc}) of the semiconductor model with a dc field. Vertical lines indicate $E_0 = U$ and $U/2$. Here, $U = 8.0, \beta = 2.0, \Gamma = 0.06$.

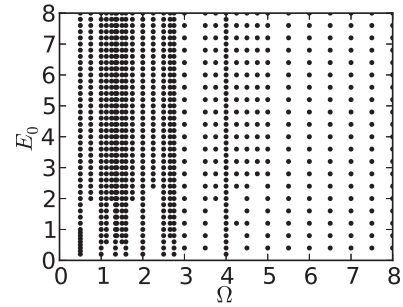

FIG. 17. Data points used for Figs. 7 and 11.

over all states. Then we can remove the index α, β in Eq. (A8) and the definition of the Green's functions becomes Eq. (A9) averaged over different Floquet states. In the present case, the time-periodic Hamiltonian is the same for the left and right systems and we can write $G_R = G_L = G'$. Here we put a prime to emphasize that G' is the Green's function for the $(d-1)$-dimensional slab. This leads to the expression

$$j(t) = -2qv^2 \frac{1}{l^{d-1}} \sum_{i_\perp, j_\perp} \int_{-\infty}^{t} d\bar{t} \left\{ G'^{<}_{i_\perp j_\perp}(\bar{t},t) G'^{>}_{j_\perp i_\perp}(t,\bar{t}) - G'^{>}_{i_\perp j_\perp}(\bar{t},t) G'^{<}_{j_\perp i_\perp}(t,\bar{t}) \right\} e^{-i\int_{\bar{t}}^{t} dt' E(t')} + \text{H.c.} \quad \text{(A10)}$$

On the other hand, since we are in the large-d limit, G' can be replaced by G in the full d-dimensional bulk. Expressing Eq. (A10) in terms of the momentum in the $(d-1)$-dimensional space and replacing G' with G, we obtain Eq. (18).

Now we further simplify Eq. (A10) by only considering the process where $i_\perp = j_\perp$. Physically this represents the contribution to the current at a certain junction between L and R by an electron that hopped through the same junction. Finally taking account of $v = \frac{v^*}{2\sqrt{d}}$ and the contribution from all directions, we obtain Eq. (19).

APPENDIX B: SEMICONDUCTOR MODEL

In order to clarify the effects associated with correlations, we consider a semiconductor model described by

$$H_{\text{semi}}(t) = -\sum_{\langle i,j\rangle,\alpha} v^{\alpha}_{ij}(t) c^{\dagger}_{i\alpha} c_{j\alpha} - \sum_{\langle i,j\rangle} v^{cv}_{ij}(t) (c^{\dagger}_{ic} c_{jv} + c^{\dagger}_{iv} c_{jc}) + \sum_{i,\alpha} D_\alpha c^{\dagger}_{i\alpha} c_{i\alpha}. \quad \text{(B1)}$$

Here $\alpha = c, v$ is the orbital index and we consider one valence band and one conduction band, which correspond to the lower and upper Hubbard bands, respectively. $D_c = -D_v = U/2$ is the crystal field. In order to mimic the fact that, in the Hubbard model, doublons and holons are created at neighboring sites by the hopping of an electron, we consider a transfer integral between neighboring sites in the semiconductor model. The effect of the field is taken into account through the Peierls substitution. We consider the NESS of the system coupled to a free electron bath, choosing $v^c = -v^v = v^{vc} = 0.5v$ and a hypercubic lattice.

In Fig. 15, we show the spectrum $[A(\omega) = (A_c(\omega) + A_v(\omega))/2]$ and occupation $[N(\omega) = (N_c(\omega) + N_v(\omega))/2]$ for the dc field. One can observe the Wannier-Stark peaks emanating from the valence and conduction bands. On the other hand, there is no signature of the peak at $\omega = \pm\frac{3}{2}U \mp 2E$, which demonstrates that many-body effects cause the appearance of this peak in the Mott insulating system.

In Fig. 16, we show the number of charge carriers ($n_c + \bar{n}_v \equiv c^{\dagger}_{i,c} c_{i,c} + c_{i,v} c^{\dagger}_{i,v}$) and the induced dc current. One can observe clear peaks at the resonances $\Omega = U/n$, as in the Mott insulator. However, the structure at $\Omega = 2U/3$ is missing, which is consistent with the absence of $\omega = \pm\frac{3}{2}U \mp 2E$ sidebands and supports the interpretation that this structure comes from many-body effects.

APPENDIX C: DATA POINTS

Because of the strong dependence on frequency and field strength in the crossover regime, we explicitly show the data points used to draw Figs. 7 and 11. Simulations were performed for the points shown in Fig. 17 and the remaining parameter values were obtained by linear interpolation.

[1] C. Giannetti, M. Capone, D. Fausti, M. Fabrizio, F. Parmigiani, and D. Mihailovic, Adv. Phys. **65**, 58 (2016).
[2] T. Oka and H. Aoki, Phys. Rev. B **79**, 081406 (2009).
[3] H. Okamoto, H. Matsuzaki, T. Wakabayashi, Y. Takahashi, and T. Hasegawa, Phys. Rev. Lett. **98**, 037401 (2007).
[4] S. Wall, D. Brida, S. R. Clark, H. P. Ehrke, D. Jaksch, A. Ardavan, S. Bonora, H. Uemura, Y. Takahashi, T. Hasegawa, H. Okamoto, G. Cerullo, and A. Cavalleri, Nat. Phys. **7**, 114 (2010).
[5] S. Iwai, M. Ono, A. Maeda, H. Matsuzaki, H. Kishida, H. Okamoto, and Y. Tokura, Phys. Rev. Lett. **91**, 057401 (2003).
[6] H. Okamoto, T. Miyagoe, K. Kobayashi, H. Uemura, H. Nishioka, H. Matsuzaki, A. Sawa, and Y. Tokura, Phys. Rev. B **83**, 125102 (2011).
[7] Y. Taguchi, T. Matsumoto, and Y. Tokura, Phys. Rev. B **62**, 7015 (2000).

[8] B. Mayer, C. Schmidt, A. Grupp, J. Bühler, J. Oelmann, R. E. Marvel, R. F. Haglund, T. Oka, D. Brida, A. Leitenstorfer, and A. Pashkin, Phys. Rev. B **91**, 235113 (2015).

[9] H. Yamakawa, T. Miyamoto, T. Morimoto, T. Terashige, H. Yada, N. Kida, M. Suda, H. M. Yamamoto, R. Kato, K. Miyagawa, K. Kanoda, and H. Okamoto, Nat. Mater. **16**, 1100 (2017).

[10] A. Takahashi, H. Gomi, and M. Aihara, Phys. Rev. Lett. **89**, 206402 (2002).

[11] T. Oka, R. Arita, and H. Aoki, Phys. Rev. Lett. **91**, 066406 (2003).

[12] H. Matsueda, T. Tohyama, and S. Maekawa, Phys. Rev. B **70**, 033102 (2004).

[13] T. Oka and H. Aoki, Phys. Rev. Lett. **95**, 137601 (2005).

[14] N. Maeshima and K. Yonemitsu, J. Phys. Soc. Jpn. **74**, 2671 (2005).

[15] T. Oka and H. Aoki, Phys. Rev. B **78**, 241104 (2008).

[16] A. Takahashi, H. Itoh, and M. Aihara, Phys. Rev. B **77**, 205105 (2008).

[17] T. Oka, Phys. Rev. B **86**, 075148 (2012).

[18] Z. Lenarčič and P. Prelovšek, Phys. Rev. Lett. **108**, 196401 (2012).

[19] F. Heidrich-Meisner, I. González, K. A. Al-Hassanieh, A. E. Feiguin, M. J. Rozenberg, and E. Dagotto, Phys. Rev. B **82**, 205110 (2010).

[20] K. Shinjo and T. Tohyama, Phys. Rev. B **96**, 195141 (2017).

[21] G. Mazza, A. Amaricci, M. Capone, and M. Fabrizio, Phys. Rev. B **91**, 195124 (2015).

[22] M. Eckstein, T. Oka, and P. Werner, Phys. Rev. Lett. **105**, 146404 (2010).

[23] M. Eckstein and P. Werner, Phys. Rev. B **84**, 035122 (2011).

[24] M. Eckstein and P. Werner, Phys. Rev. Lett. **110**, 126401 (2013).

[25] M. Eckstein and P. Werner, J. Phys.: Conf. Ser. **427**, 012005 (2013).

[26] P. Werner and M. Eckstein, Europhys. Lett. **109**, 37002 (2015).

[27] A. Herrmann, Y. Murakami, M. Eckstein, and P. Werner, Europhys. Lett. **120**, 57001 (2017).

[28] F. Peronaci, M. Schiró, and O. Parcollet, Phys. Rev. Lett. **120**, 197601 (2018).

[29] T. Mori, T. Kuwahara, and K. Saito, Phys. Rev. Lett. **116**, 120401 (2016).

[30] T. Kuwahara, T. Mori, and K. Saito, Ann. Phys. **367**, 96 (2016).

[31] M. Eckstein, J. Mentink, and P. Werner, arXiv:1703.03269 (unpublished).

[32] C. Aron, Phys. Rev. B **86**, 085127 (2012).

[33] A. V. Joura, J. K. Freericks, and T. Pruschke, Phys. Rev. Lett. **101**, 196401 (2008).

[34] N. Tsuji, T. Oka, and H. Aoki, Phys. Rev. B **78**, 235124 (2008).

[35] W.-R. Lee and K. Park, Phys. Rev. B **89**, 205126 (2014).

[36] J. Li, C. Aron, G. Kotliar, and J. E. Han, Phys. Rev. Lett. **114**, 226403 (2015).

[37] G. Mazza, A. Amaricci, M. Capone, and M. Fabrizio, Phys. Rev. Lett. **117**, 176401 (2016).

[38] J. Li, C. Aron, G. Kotliar, and J. E. Han, Nano Lett. **17**, 2994 (2017).

[39] P. Schmidt and H. Monien, arXiv:cond-mat/0202046 (unpublished).

[40] N. Tsuji, T. Oka, and H. Aoki, Phys. Rev. Lett. **103**, 047403 (2009).

[41] T. Mikami, S. Kitamura, K. Yasuda, N. Tsuji, T. Oka, and H. Aoki, Phys. Rev. B **93**, 144307 (2016).

[42] Y. Murakami, M. Eckstein, and P. Werner, Phys. Rev. Lett. **121**, 057405 (2018).

[43] H. Aoki, N. Tsuji, M. Eckstein, M. Kollar, T. Oka, and P. Werner, Rev. Mod. Phys. **86**, 779 (2014).

[44] Y. Murakami, N. Tsuji, M. Eckstein, and P. Werner, Phys. Rev. B **96**, 045125 (2017).

[45] M. Eckstein and P. Werner, Phys. Rev. B **82**, 115115 (2010).

[46] M. E. Sorantin, A. Dorda, K. Held, and E. Arrigoni, Phys. Rev. B **97**, 115113 (2018).

[47] A. Georges, G. Kotliar, W. Krauth, and M. J. Rozenberg, Rev. Mod. Phys. **68**, 13 (1996).

[48] Y. Meir and N. S. Wingreen, Phys. Rev. Lett. **68**, 2512 (1992).

[49] W. Metzner, P. Schmit, and D. Vollhardt, Phys. Rev. B **45**, 2237 (1992).

[50] J. K. Freericks, Phys. Rev. B **77**, 075109 (2008).

[51] T. Ishikawa, Y. Sagae, Y. Naitoh, Y. Kawakami, H. Itoh, K. Yamamoto, K. Yakushi, H. Kishida, T. Sasaki, S. Ishihara, Y. Tanaka, K. Yonemitsu, and S. Iwai, Nat. Commun. **5**, 5528 (2014).

[52] A. Ono, H. Hashimoto, and S. Ishihara, Phys. Rev. B **95**, 085123 (2017).

[53] M. Bukov, M. Kolodrubetz, and A. Polkovnikov, Phys. Rev. Lett. **116**, 125301 (2016).

[54] L. Keldysh, JETP **20**, 1207 (1965).

[55] P. B. Corkum, Phys. Rev. Lett. **71**, 1994 (1993).

[56] M. Lewenstein, P. Balcou, M. Y. Ivanov, A. L'Huillier, and P. B. Corkum, Phys. Rev. A **49**, 2117 (1994).

[57] A. L. Cavalieri, N. Müller, T. Uphues, V. S. Yakovlev, A. Baltuska, B. Horvath, B. Schmidt, L. Blümel, R. Holzwarth, S. Hendel, Nature (London) **449**, 1029 (2007).

[58] F. Krausz and M. Ivanov, Rev. Mod. Phys. **81**, 163 (2009).

[59] D. Golde, T. Meier, and S. W. Koch, Phys. Rev. B **77**, 075330 (2008).

[60] S. Ghimire, A. D. DiChiara, E. Sistrunk, P. Agostini, L. F. DiMauro, and D. A. Reis, Nat. Phys. **7**, 138 (2010).

[61] O. Schubert, M. Hohenleutner, F. Langer, B. Urbanek, C. Lange, U. Huttner, D. Golde, T. Meier, M. Kira, S. W. Koch, and R. Huber, Nat. Photon. **8**, 119 (2014).

[62] M. Hohenleutner, F. Langer, O. Schubert, M. Knorr, U. Huttner, S. W. Koch, M. Kira, and R. Huber, Nature (London) **523**, 572 (2015).

[63] T. T. Luu, M. Garg, S. Y. Kruchinin, A. Moulet, M. T. Hassan, and E. Goulielmakis, Nature (London) **521**, 498 (2015).

[64] A. F. Kemper, B. Moritz, J. K. Freericks, and T. P. Devereaux, New J. Phys. **15**, 023003 (2013).

[65] T. Higuchi, M. I. Stockman, and P. Hommelhoff, Phys. Rev. Lett. **113**, 213901 (2014).

[66] G. Vampa, C. R. McDonald, G. Orlando, D. D. Klug, P. B. Corkum, and T. Brabec, Phys. Rev. Lett. **113**, 073901 (2014).

[67] G. Vampa, C. R. McDonald, G. Orlando, P. B. Corkum, and T. Brabec, Phys. Rev. B **91**, 064302 (2015).

[68] G. Vampa, T. J. Hammond, N. Thire, B. E. Schmidt, F. Legare, C. R. McDonald, T. Brabec, and P. B. Corkum, Nature (London) **522**, 462 (2015).

[69] F. Langer, M. Hohenleutner, C. P. Schmid, C. Poellmann, P. Nagler, T. Korn, C. Schüller, M. S. Sherwin, U. Huttner, J. T. Steiner, S. W. Koch, M. Kira, and R. Huber, Nature (London) **533**, 225 (2016).

[70] G. Ndabashimiye, S. Ghimire, M. Wu, D. A. Browne, K. J. Schafer, M. B. Gaarde, and D. A. Reis, Nature (London) **534**, 520 (2016).
[71] H. Liu, Y. Li, Y. S. You, S. Ghimire, T. F. Heinz, and D. A. Reis, Nat. Phys. **13**, 262 (2016).
[72] Y. S. You, D. A. Reis, and S. Ghimire, Nat. Phys. **13**, 345 (2017).
[73] T. Otobe, Phys. Rev. B **94**, 235152 (2016).
[74] T. T. Luu and H. J. Wörner, Phys. Rev. B **94**, 115164 (2016).
[75] T. Tamaya, A. Ishikawa, T. Ogawa, and K. Tanaka, Phys. Rev. Lett. **116**, 016601 (2016).
[76] N. Yoshikawa, T. Tamaya, and K. Tanaka, Science **356**, 736 (2017).
[77] T. Ikemachi, Y. Shinohara, T. Sato, J. Yumoto, M. Kuwata-Gonokami, and K. L. Ishikawa, Phys. Rev. A **95**, 043416 (2017).
[78] N. Tancogne-Dejean, O. D. Mücke, F. X. Kärtner, and A. Rubio, Phys. Rev. Lett. **118**, 087403 (2017).
[79] N. Tancogne-Dejean, O. D. Mücke, F. X. Kärtner, and A. Rubio, Nat. Commun. **8**, 745 (2017).
[80] R. E. F. Silva, I. V. Blinov, A. N. Rubtsov, O. Smirnova, and M. Ivanov, Nat. Photon. **12**, 266 (2018).
[81] N. Tancogne-Dejean, M. A. Sentef, and A. Rubio, arXiv:1712.01067 (unpublished).
[82] G. Jotzu, M. Messer, R. Desbuquois, M. Lebrat, T. Uehlinger, D. Greif, and T. Esslinger, Nature (London) **515**, 237 (2014).
[83] M. A. Sentef, M. Claassen, A. F. Kemper, B. Moritz, T. Oka, J. K. Freericks, and T. P. Devereaux, Nat. Commun. **6**, 7047 (2015).
[84] J. H. Mentink, K. Balzer, and M. Eckstein, Nat. Commun. **6**, 6708 (2015).
[85] K. Takasan, M. Nakagawa, and N. Kawakami, Phys. Rev. B **96**, 115120 (2017).
[86] T. Oka and S. Kitamura, arXiv:1804.03212 (unpublished).
[87] F. Görg, M. Messer, K. Sandholzer, G. Jotzu, R. Desbuquois, and T. Esslinger, Nature (London) **553**, 481 (2018).